8

Thermal Transport in Metallic Porous Media

Z.G. Qu[1], H.J. Xu[1], T.S. Wang[1], W.Q. Tao[1] and T.J. Lu[2]
[1]*Key Laboratory of Thermal Fluid Science and Engineering, MOE*
[2]*Key Laboratory of Strength and Vibration, MOE of Xi'an Jiaotong University in Xi'an, China*

1. Introduction

Using porous media to extend the heat transfer area, improve effective thermal conductivity, mix fluid flow and thus enhance heat transfer is an enduring theme in the field of thermal fluid science. According to the internal connection of neighbouring pore elements, porous media can be classified as the consolidated and the unconsolidated. For thermal purposes, the consolidated porous medium is more attractive as its thermal contact resistance is considerably lower. Especially with the development of co-sintering technique, the consolidated porous medium made of metal, particularly the metallic porous medium, gradually exhibits excellent thermal performance because of many unique advantages such as low relative density, high strength, high surface area per unit volume, high solid thermal conductivity, and good flow-mixing capability (Xu et al., 2011b). It may be used in many practical applications for heat transfer enhancement, such as catalyst supports, filters, bio-medical implants, heat shield devices for space vehicles, novel compact heat exchangers, and heat sinks, et al. (Banhart, 2011; Xu et al., 2011a, 2011b, 2011c).

The metallic porous medium to be introduced in this chapter is metallic foam with cellular micro-structure (porosity greater than 85%). It shows great potential in the areas of acoustics, mechanics, electricity, fluid dynamics and thermal science, especially as an important porous material for thermal aspect. Principally, metallic foam is classified into open-cell foam and close-cell foam according to the morphology of pore element. Close-cell metallic foams are suitable for thermal insulation, whereas open-cell metallic foams are often used for heat transfer enhancement. Open-cell metallic foam is only discussed for thermal performance. Figure 1(a) and 1(b) show the real structure of copper metallic foam

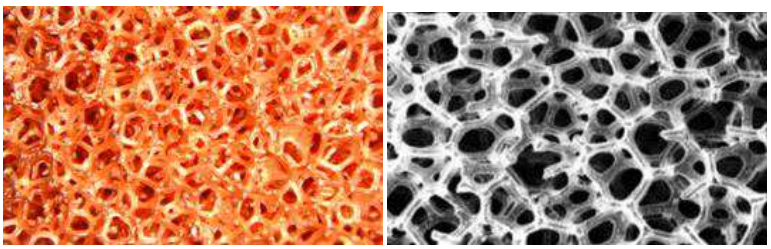

(a) (b)

Fig. 1. Metallic foams picture: (a) sample; (b) SEM (scanning electron microscope)

and its SEM image respectively It can be noted that metallic foams own three-dimensional space structures with interconnection between neighbouring pore elements (cell). The morphology structure is defined as porosity (ε) and pore density (ω), wherein pore density is the pore number in a unit length or pores per inch (PPI).

In the last two decades, there have been continuous concerns on the flow and heat transfer properties of metallic foam. Lu et al. (Lu et al., 1998) performed a comprehensive investigation of flow and heat transfer in metallic foam filled parallel-plate channel using the fin-analysis method. Calmidi and Mahajan (Calmidi & Mahajan, 2000) conducted experiments and numerical studies on forced convection in a rectangular duct filled with metallic foams to analyze the effects of thermal dispersion and local non-thermal equilibrium with quantified thermal dispersion conductivity, k_d, and interstitial heat transfer coefficient, h_{sf}. Lu and Zhao et al. (Lu et al., 2006; Zhao et al., 2006) performed analytical solution for fully developed forced convective heat transfer in metallic foam fully filled inner-pipe and annulus of tube-in-tube heat exchangers. They found that the existence of metallic foams can significantly improve the heat transfer coefficient, but at the expense of large pressure drop. Zhao et al. (Zhao et al., 2005) conducted experiments and numerical studies on natural convection in a vertical cylindrical enclosure filled with metallic foams; they found favourable correlation between numerical and experimental results. Zhao et al. (Zhao & Lu et al., 2004) experimented on and analyzed thermal radiation in highly porous metallic foams and gained favourable results between the analytical prediction and experimental data. Zhao et al. (Zhao & Kim et al., 2004) performed numerical simulation and experimental study on forced convection in metallic foam fully filled parallel-plate channel and obtained good results. Boomsma and Poulikakos (Boomsma & Poulikakos, 2011) proposed a three-dimensional structure for metallic foam and obtained the empirical correlation of effective thermal conductivity based on experimental data. Calmidi (Calmidi, 1998) performed an experiment on flow and thermal transport phenomena in metallic foams and proposed a series of empirical correlations of fibre diameter d_f, pore diameter d_P, specific surface area a_{sf}, permeability K, inertia coefficient C_I, and effective thermal conductivity k_e. Simultaneously, a numerical simulation was conducted based on the correlations developed and compared with the experiment with reasonable results. Overall, metallic foam continues to be a good candidate for heat transfer enhancement due to its excellent thermal performance despite its high manufacturing cost.

For thermal modeling in metallic foams with high solid thermal conductivities, the local thermal equilibrium model, specifically the one-energy equation model, no longer satisfies the modelling requirements. Lee and Vafai (Lee & Vafai, 1999) addressed the viewpoint that for solid and fluid temperature differentials in porous media, the local thermal non-equilibrium model (two-energy equation model) is more accurate than the one-equation model when the difference between thermal conductivities of solid and fluid is significant, as is the case for metallic foams. Similar conclusions can be found in Zhao (Zhao et al., 2005) and Phanikumar and Mahajan (Phanikumar & Mahajan, 2002). Therefore, majority of published works concerning thermal modelling of porous foam are performed with two equation models.

In this chapter, we report the recent progress on natural convection on metallic foam sintered surface, forced convection in ducts fully/partially filled with metallic foams, and modelling of film condensation heat transfer on a vertical plate embedded in infinite metallic foams. Effects of morphology and geometric parameters on transport performance

are discussed, and a number of useful suggestions are presented as well in response to engineering demand.

2. Natural convection on surface sintered with metallic porous media

Due to the use of co-sintering technique, effective thermal resistance of metallic porous media is very high, which satisfies the heat transfer demand of many engineering applications such as cooling of electronic devices. Natural convection on surface sintered with metallic porous media has not been investigated elsewhere. Natural convection in an enclosure filled with metallic foams or free convection on a surface sintered with metallic foams has been studied to a certain extent (Zhao et al., 2005; Phanikumar & Mahajan, 2002; Jamin & Mohamad, 2008).

The test rig of natural convection on inclined surface is shown in Fig. 2. The experiment system is composed of plexiglass house, stainless steel holder, tripod, insulation material, electro-heating system, data acquisition system, and test samples. The dashed line in Fig. 2 represents the plexiglass frame. This experiment system is prepared for metallic foam sintered plates. The intersection angle of the plate surface and the gravity force is set as the inclination angle θ. The Nusselt number due to convective heat transfer (with subscript 'conv') can be calculated as:

$$Nu_{\mathrm{conv}} = h_{\mathrm{conv}} \frac{L}{k} = \frac{\phi_{\mathrm{conv}}}{A\left(T_{\mathrm{w}} - T_{\infty}\right)} \frac{L}{k} = \frac{\phi - \mathrm{E}\sigma\left({T_{\mathrm{rad}}}^{4} - {T_{\infty}}^{4}\right) A_{\mathrm{rad}}}{A\left(T_{\mathrm{w}} - T_{\infty}\right)} \frac{L}{k} . \tag{1}$$

where h, L, k, ϕ, A, Tw, T_{∞}, E and σ respectively denotes heat transfer coefficient, length, thermal conductivity, heat, area, wall temperature, surrounding temperature, emissive power and Boltzmann constant. The subscript 'rad' refers to 'radiation'.

Meanwhile, the average Nusselt number due to the combined convective and radiative heat transfer can be expressed as follows:

$$Nu_{\mathrm{av}} = h_{\mathrm{av}} \frac{L}{k} = \frac{\phi}{A(T_{\mathrm{w}} - T_{\infty})} \frac{L}{k} . \tag{2}$$

In Eq.(2), the subscript 'av' denotes 'average'.

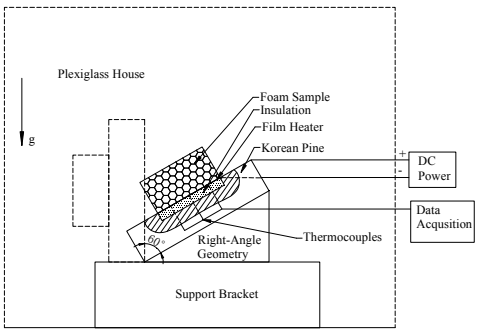

Fig. 2. Test rig of natural convection on inclined surface sintered with metallic foams

Experiment results of the conjugated radiation and natural convective heat transfer on wall surface sintered with open-celled metallic foams at different inclination angles are presented. The metal foam test samples have the same length and width of 100 mm, but different height of 10 mm and 40 mm. To investigate the coupled radiation and natural convection on the metal foam surface, a black paint layer with thickness of 0.5 mm and emissivity 0.96 is painted on the surface of the metal foam surface for the temperature testing with infrared camera. Porosity is 0.95, while pore density is 10 PPI.

Figure 3(a) shows the comparison between different experimental data, several of which were obtained from existing literature. The present result without paint agrees well with existing experimental data (Sparrow & Gregg, 1956; Fujii T. & Fujii M., 1976; Churchil & Ozoe, 1973). However, experimental result with paint is higher than unpainted metal foam block. This is attributed to the improved emissivity of black paint layer of painted surface.

Figure 3(b) presents effect of inclination angle on the average Nusselt number for two thicknesses of metallic foams (δ / L=0.1 and 0.4). As inclination angle increases from 0° (vertical position) to 90° (horizontal position), heat transferred in convective model initially increases and subsequently decreases. The maximum value is between 60° and 80°. Hence, overall heat transfer increases initially and remains constant as inclination angle increases.

To investigate the effect of radiation on total heat transfer, a ratio of the total heat transfer occupied by the radiation is introduced in this chapter, as shown below:

$$\mathrm{R} = \frac{\phi_{\mathrm{rad}}}{\phi} . \tag{3}$$

Figure 3(c) provides the effect inclination angle on R for different foam samples (δ / L=0.1 and 0.4). In the experiment scope, the fraction of radiation in the total heat transfer is in the range of 33.8%–41.2%. For the metal foam sample with thickness of 10 mm, R is decreased as the inclination angle increases. However, with a thickness of 40 mm, R decreases initially and eventually increases as the inclination angle increases, reaching the minimum value of approximately 75°.

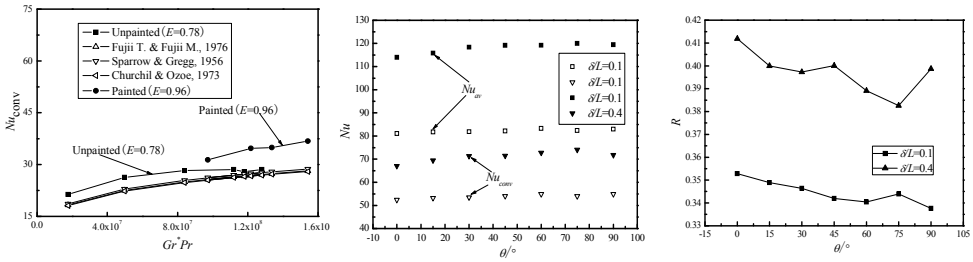

(a) (b) (c)

Fig. 3. Experimental results: (a) comparison with existing data; (b) effect of inclination angle on heat transfer; (c) effect of inclination angle on R

Figure 4 shows the infrared result of temperature distribution on the metallic foam surface with different foam thickness. It can be seen that the foam block with larger thickness has less homogeneous temperature distribution.

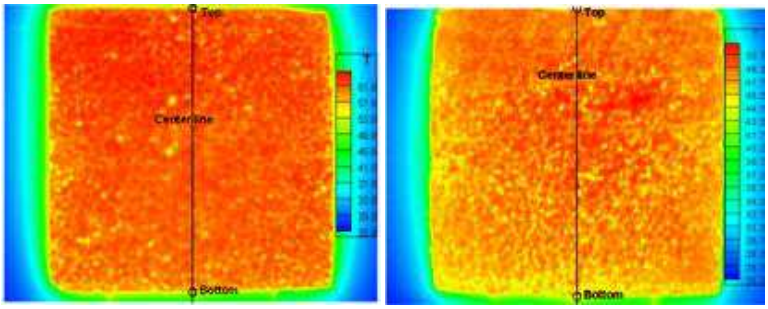

(a) (b)

Fig. 4. Temperature distribution of metallic foam surface predicted by infrared rays: (a) δ/L=0.1; (b) δ/L=0.4

3. Forced convection modelling in metallic foams

Research on thermal modeling of internal forced convective heat transfer enhancement using metallic foams is presented here. Several analytical solutions are shown below as benchmark for the improvement of numerical techniques. The Forchheimer model is commonly used for establishing momentum equations of flow in porous media. After introducing several empirical parameters of metallic foams, it is expressed for steady flow as:

$$\frac{\rho_f}{\varepsilon^2}\left\langle\left(\vec{U}\cdot\nabla\right)\vec{U}\right\rangle=-\nabla p_f+\frac{\mu_f}{\varepsilon}\nabla^2\left\langle\vec{U}\right\rangle-\frac{\mu_f}{K}\left\langle\vec{U}\right\rangle-\frac{\rho_f C_I}{\sqrt{K}}\left[\left\langle\vec{U}\right\rangle\cdot\left\langle\vec{U}\right\rangle\right]J\,. \tag{4}$$

where ρ, p, μ, K, C_I, $\vec{U}$ is density, pressure, kinematic viscousity, permeability, inertial coefficient and velocity vector, respectively. And J is the unit vector along pore velocity vector $J=\overrightarrow{U_P}/\left|\overrightarrow{U_P}\right|$. The angle bracket means the volume averaged value. The term in the left-hand side of Eq. (4) is the advective term. The terms in the right-hand side are pore pressure gradient, viscous term (i.e., Brinkman term), Darcy term (microscopic viscous shear stress), and micro-flow development term (inertial term), respectively. When porosity approaches 1, permeability becomes very large and Eq. (4) is converted to the classical Navier-Stokes equation.

Thermal transport in porous media owns two basic models: local thermal equilibrium model (LTE) and local thermal non-equilibrium model (LNTE). The former with one-energy equation treats the local temperature of solid and fluid as the same value while the latter has two-energy equations taking into account the difference between the temperatures of solid and fluid. They take the following forms [Eq. (5) for LTE and Eqs. (6a-6b) for LNTE]:

$$\left\langle\rho_f\right\rangle c_f\left\langle\vec{U}\right\rangle\nabla\left\langle T\right\rangle=\nabla\left[\left(k_{fe}+k_d\right)\nabla\left\langle T\right\rangle\right]. \tag{5}$$

$$0=\nabla\left[k_{se}\nabla\left\langle T_s\right\rangle\right]-h_{sf}a_{sf}\left(T_s-T_f\right). \tag{6a}$$

$$\left\langle\rho_f\right\rangle c_f\left\langle\vec{U}\right\rangle\nabla\left\langle T_f\right\rangle=\nabla\left[k_{fe}\nabla\left\langle T_f\right\rangle\right]+h_{sf}a_{sf}\left(T_s-T_f\right). \tag{6b}$$

Subscripts 'f', 's', 'fe', 'se', 'd' and 'sf' respectively denotes 'fluid', 'solid', 'effective value of fluid', 'effective value of solid', 'dispersion' and 'solid and fluid'. ***T*** is temperature variable.
As stated above, Lee and Vafai (Lee & Vafai, 1999) indicated that the LNTE model is more accurate than the LTE model when the difference between solid and fluid thermal conductivities is significant. This is true in the case of metallic foams, in which difference between solid and fluid phases is often two orders of magnitudes or more. Thus, LNTE model with two-energy equations (also called two-equation model) is employed throughout this chapter.
For modeling forced convective heat transfer in metallic foams, the metallic foams are assumed to be isotropic and homogeneous. For analytical simplification, the flow and temperature fields of impressible fluid are fully developed, with thermal radiation and natural convection ignored. Simultaneously, thermal dispersion is negligible due to high solid thermal conductivity of metallic foams (Calmidi & Mahajan, 2000; Lu et al., 2006; Dukhan, 2009). As a matter of convenience, the angle brackets representing the volume-averaging qualities for porous medium are dropped hereinafter.

3.1 Fin analysis model

As fin analysis model is a very simple and useful method to obtain temperature distribution, fin theory-based heat transfer analysis is discussed here and a modified fin analysis method of present authors (Xu et al., 2011a) for metallic foam filled channel is introduced. A comparison between results of present and conventional models is presented.
Fin analysis method for heat transfer is originally adopted for heat dissipation body with extended fins. It is a very simple and efficient method for predicting the temperature distribution in these fins. It was first introduced to solve heat transfer problems in porous media by Lu et al. in 1998 (Lu et al., 1998). As presented, the heat transfer results with fin analysis exhibit good trends with variations of foam morphology parameters. However, it has been pointed out that this method may overpredict the heat transfer performance. This fin analysis method treats the velocity and temperature of fluid flowing through the porous foam as uniform, significantly overestimating the heat transfer result. With the assumption of cubic structure composed of cylinders, fin analysis formula of Lu et al. (Lu et al., 1998) is expressed as:

$$\frac{\partial^2 T_s(x,y)}{\partial y^2} - \frac{4h_{sf}}{k_s d_f}\left[T_s(x,y) - T_{f,b}(x)\right] = 0 . \tag{7}$$

where (x,y) is the Cartesian coordinates and d_f is the fibre diameter. The subscript 'f,b' denotes 'bulk mean value of fluid'.
In the previous model (Lu et al., 1998), heat conduction in the cylinder cell is only considered and the surface area is taken as outside surface area of cylinders with thermal conductivity k_s. Based on the assumption, thermal resistance in the fin is artificially reduced, leading to the previous fin method that overestimates heat transfer. Fluid with temperature $T_{f,b}(x)$ flows through the porous channel. The fluid heat conduction in the foam is considered together with the solid heat conduction. The effective thermal conductivity k_e and extended surface area density of porous foam a_{sf} instead of k_s and surface area of solid cylinders are applied to gain the governing equation. The modified heat conduction equation proposed by present authors (Xu et al., 2011a) is as follows:

$$\frac{\partial^2 T_{e,f}(x,y)}{\partial y^2} - \frac{h_{sf} a_{sf}}{k_e}\left[T_{e,f}(x,y) - T_{f,b}(x)\right] = 0. \tag{8}$$

Temperature $T_{e,f}(x)$ in Eq. (8) representing the temperature of porous foam is defined as the equivalent foam temperature. With the constant heat flux condition, equivalent foam temperature, and Nusselt number are obtained in Eq. (9) and Eq. (10):

$$T_{e,f}(x,y) = T_{f,b}(x) + q_w \cosh(my) / \left[mk_e \sinh(mH)\right]. \tag{9}$$

$$Nu = \frac{q_w}{T_w(x) - T_{f,b}(x)} \frac{4H}{k_f} = \frac{q_w}{T_{e,f}(x,0) - T_{f,b}(x)} \frac{4H}{k_f} = 4mH \cdot \frac{k_e}{k_f} \cdot \tanh(mH). \tag{10}$$

where q_w is the wall heat flux and H is the half width of the parallel-plate channel. The fin efficiency m is calculated with $m=h_{sf}a_{sf}/k_e$.

To verify the improvement of the present modified fin analysis model for heat transfer in metallic foams, the comparison among the present fin model, previous fin model (Lu et al., 1998), and the analytical solution presented in Section 3.2 is shown in Fig. 5. Figure 5(a) presents the comparison between the Nusselt number results predicted by present modified fin model, previous fin model (Lu et al., 1998), and analytical solution in Section 3.2. Evidently, the present modified fin model is closer to the analytical solution. It can replace the previous fin model (Lu et al., 1998) to estimate heat transfer in porous media with improved accuracy. Only the heat transfer results of the present modified fin model and analytical solution in Section 3.2 are compared in Fig. 5(b). It is noted that when k_f/k_s is sufficiently small, the present modified fin model can coincide with the analytical solution. The difference between the two gradually increases as k_f/k_s increases.

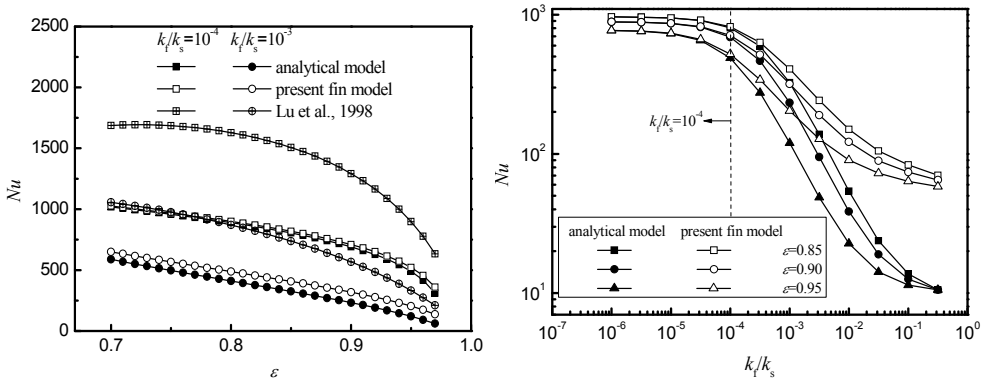

(a) (b)

Fig. 5. Comparisons of Nu (a) among present modified fin model, previous fin model (Lu et al., 1998), and analytical solution in Section 3.2.1 (ω=10 PPI, H=0.005 m, u_m=1 m·s^{-1}); (b) between present modified fin model and analytical solution in Section 3.2.1 (ω=10 PPI, H=0.005 m, u_m=1 m·s^{-1})

3.2 Analytical modeling

3.2.1 Metallic foam fully filled duct

In this part, fully developed forced convective heat transfer in a parallel-plate channel filled with highly porous, open-celled metallic foams is analytically modeled using the Brinkman-Darcy and two-equation models and the analytical results of the present authors (Xu et al., 2011a) are presented in the following. Closed-form solutions for fully developed fluid flow and heat transfer are proposed.

Figure 6 shows the configuration of a parallel-plate channel filled with metallic foams. Two infinite plates are subjected to constant heat flux q_w with height $2H$. Incompressible fluid flows through the channel with mean velocity u_m and absorbs heat imposed on the parallel plates.

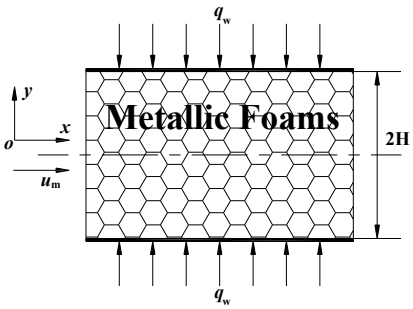

Fig. 6. Schematic diagram of metallic foam fully filled parallel-plate channel

For simplification, the angle brackets representing volume-averaged variables are dropped from Eqs. (4), (6a), and (6b). The governing equations and closure conditions are normalized with the following qualities:

$$Y=\frac{y}{H},U=\frac{u}{u_{\mathrm{m}}},P=\frac{K}{\mu_{\mathrm{f}}u_{\mathrm{m}}}\frac{\mathrm{d}p}{\mathrm{d}x},\theta_{\mathrm{s}}=\frac{T_{\mathrm{s}}-T_{\mathrm{w}}}{q_{\mathrm{w}}H/k_{\mathrm{se}}},\theta_{\mathrm{f}}=\frac{T_{\mathrm{f}}-T_{\mathrm{w}}}{q_{\mathrm{w}}H/k_{\mathrm{se}}}, \tag{11a}$$

$$Da=\frac{K}{H^2},B=\frac{k_{\mathrm{f}}}{k_{\mathrm{se}}},C=\frac{k_{\mathrm{fe}}}{k_{\mathrm{se}}},D=\frac{h_{\mathrm{sf}}a_{\mathrm{sf}}H^2}{k_{\mathrm{se}}},s=\sqrt{\varepsilon/Da},t=\sqrt{D(C+1)/C}\,. \tag{11b}$$

Empirical correlations for these parameters are listed in Table 1.

After neglecting the inertial term in Eq. (4), governing equations for problem shown in Fig. 6 can be normalized as:

$$\frac{\partial^2 U}{\partial Y^2}-s^2(U+P)=0\,. \tag{12a}$$

$$\frac{\partial^2\theta_{\mathrm{s}}}{\partial Y^2}-D(\theta_{\mathrm{s}}-\theta_{\mathrm{f}})=0\,. \tag{12b}$$

$$C\frac{\partial^2\theta_{\mathrm{f}}}{\partial Y^2}+D(\theta_{\mathrm{s}}-\theta_{\mathrm{f}})=U\,. \tag{12c}$$

Parameter	Correlation	Reference
Pore diameter d_p	$d_p = 0.0254/\omega$	Calmidi, 1998
Fibre diameter d_f	$d_f = d_p \cdot 1.18\sqrt{(1-\varepsilon)/(3\pi)}\left[1-\exp\left((\varepsilon-1)/0.04\right)\right]^{-1}$	Calmidi, 1998
Specific surface area a_{sf}	$a_{sf} = 3\pi d_f\left[1-e^{-\left((1-\varepsilon)/0.04\right)}\right]/\left(0.59 d_p\right)^2$	Zhao et al., 2001
Permeability K	$K = 0.00073(1-\varepsilon)^{-0.224}\left(d_f/d_p\right)^{-1.11} d_p^2$	Calmidi, 1998
Local heat transfer coefficient h_{sf}	$h_{sf} = \begin{cases} 0.76 Re_d^{0.4} Pr^{0.37} k_f/d, & (1 \le Re_d \le 40) \\ 0.52 Re_d^{0.5} Pr^{0.37} k_f/d, & (40 \le Re_d \le 10^3) \\ 0.26 Re_d^{0.6} Pr^{0.37} k_f/d, & (10^3 \le Re_d \le 2\times 10^5) \end{cases}$ $Re_d = \rho_f u d/\mu_f$	Lu et al., 2006
Effective thermal conductivity k_e	$R_A = \dfrac{4\lambda}{\left(2e^2+\pi\lambda(1-e)\right)k_s + \left(4-2e^2-\pi\lambda(1-e)\right)k_f}$ $R_B = \dfrac{(e-2\lambda)^2}{(e-2\lambda)e^2 k_s + \left(2e-4\lambda-(e-2\lambda)e^2\right)k_f}$ $R_C = \dfrac{\left(\sqrt{2}-2e\right)^2}{2\pi\lambda^2\left(1-2\sqrt{2}e\right)k_s + 2\left(\sqrt{2}-2e-\pi\lambda^2\left(1-2\sqrt{2}e\right)\right)k_f}$ $R_D = \dfrac{2e}{e^2 k_s + \left(4-e^2\right)k_f}$ $\lambda = \sqrt{\dfrac{\sqrt{2}\left(2-(5/8)e^3\sqrt{2}-2\varepsilon\right)}{\pi\left(3-4\sqrt{2}e-e\right)}},\ e = 0.339$ $k_e = \dfrac{1}{\sqrt{2}\left(R_A+R_B+R_C+R_D\right)}\quad k_{se} = k_e\big\|_{k_f=0},\ k_{fe} = k_e\big\|_{k_s=0}$	Boomsma & Poulikakos, 2001

Table 1. Semi-empirical correlations of parameters for metallic foams

The dimensionless closure conditions can likewise be derived as follows:

$$Y = 0, \frac{\partial U}{\partial Y} = \frac{\partial \theta_s}{\partial Y} = \frac{\partial \theta_f}{\partial Y} = 0; Y = 1, U = 0, \theta_s = \theta_f = 0. \tag{13}$$

Thus, the dimensionless velocity profile is expressed by the hyperbolic functions:

$$U = P\left[\cosh(sY)/\cosh(s) - 1\right]. \tag{14a}$$

$$P = \frac{1}{\tanh(s)/s - 1}. \tag{14b}$$

Meanwhile, dimensionless fluid and solid temperatures can be derived as follows:

$$\theta_s + C\theta_f = P\left[\frac{\cosh(sY)}{s^2\cosh(s)} - \frac{1}{2}Y^2 + \frac{1}{2} - \frac{1}{s^2}\right]. \tag{15a}$$

$$\theta_f = P\left[\frac{C\cdot s^2}{D(C+1)^2\left[C\cdot s^2 - D(C+1)\right]}\frac{\cosh(tY)}{\cosh(t)} + \frac{\left(1 - D/s^2\right)}{\left[C\cdot s^2 - D(C+1)\right]}\frac{\cosh(sY)}{\cosh(s)} - \frac{1}{2(C+1)}Y^2 + \frac{D\left(1/2 - 1/s^2\right) - 1/(C+1)}{D(C+1)}\right]. \tag{15b}$$

$$\theta_s = P\left[-\frac{C^2\cdot s^2}{D(C+1)^2\left[C\cdot s^2 - D(C+1)\right]}\frac{\cosh(tY)}{\cosh(t)} - \frac{D/s^2}{\left[C\cdot s^2 - D(C+1)\right]}\frac{\cosh(sY)}{\cosh(s)} - \frac{1}{2(C+1)}Y^2 + \frac{D\left(1/2 - 1/s^2\right) + C/(C+1)}{D(C+1)}\right]. \tag{15c}$$

The dimensionless numbers, friction factor f, and Nusselt number Nu are shown below.

$$f = \frac{\mathrm{d}p/\mathrm{d}x\cdot 4H}{\rho_f u_m^2/2} = \frac{32P}{Re\cdot Da}. \tag{16a}$$

$$Nu = \frac{q_w}{T_w - T_{f,b}}\frac{4H}{k_f} = -\frac{4}{B\cdot\theta_{f,b}}. \tag{16b}$$

In Eq. (20), the dimensionless bulk fluid temperature can be obtained using Eq. (19).

$$\theta_{f,b} = \frac{\frac{1}{A}\int_A U\theta_f \mathrm{d}A}{\frac{1}{A}\int_A U\mathrm{d}A} = \int_0^1 U\theta_f \mathrm{d}Y = P^2\left\{\frac{\left[\frac{\cosh(s+t)}{s+t} - \frac{\cosh(s-t)}{s-t}\right]C\cdot s^2}{2D(C+1)^2\left[C\cdot s^2 - D(C+1)\right]\cosh(s)\cosh(t)} + \frac{\left(1-\frac{D}{s^2}\right)\cosh(2s)}{4\left[C\cdot s^2 - D(C+1)\right]s\cdot\cosh^2(s)} + \frac{\left(1-\frac{D}{s^2}\right)\left[e^s\left(1-\frac{2}{s}+\frac{2}{s^2}\right) - e^{-s}\left(1+\frac{2}{s}+\frac{2}{s^2}\right)\right]}{4\left[C\cdot s^2 - D(C+1)\right]s\cdot\cosh^2(s)} + \frac{1}{s}\left(\frac{C\cdot s^2}{D(C+1)^2\left[C\cdot s^2 - D(C+1)\right]} + \frac{1}{2(C+1)}\right) - \frac{C\cdot s^2}{D(C+1)^2\left[C\cdot s^2 - D(C+1)\right]t} + \frac{1}{6(C+1)} + \frac{1-\frac{D}{s^2}}{\left[C\cdot s^2 - D(C+1)\right]\cosh^2(s)} - \frac{D\left(\frac{1}{2}-\frac{1}{s^2}\right) - \frac{1}{C+1}}{D(C+1)}\right\}. \tag{17}$$

The Nusselt number of the present analytical solution is compared with experiment data (Zhao & Kim, 2001) for forced convection in rectangular metallic foam filled duct [Fig. 7(a)]. As illustrated, the difference between the analytical and previous experiment results is attributed to the experimental error and omission of the dispersion effect and quadratic term in the velocity equation. Overall, the analytical and experimental results are correlated with each other, with reasonable similarities. To examine the effect of the Brinkman term, comparison between temperature profiles of the present solution and that of Lee and Vafai (Lee & Vafai, 1999) is presented in Fig. 7(b). It can be observed that temperature profiles of the two solutions are similar. In particular, the predicted temperatures for solid and fluid of Lee and Vafai (Lee & Vafai, 1999) are closer to the wall temperature than the present solution. This is due to the completely uniform cross-sectional velocity assumed for the Darcy model by Lee and Vafai (Lee & Vafai, 1999). The comparison provides another evidence for the feasibility of the present solution.

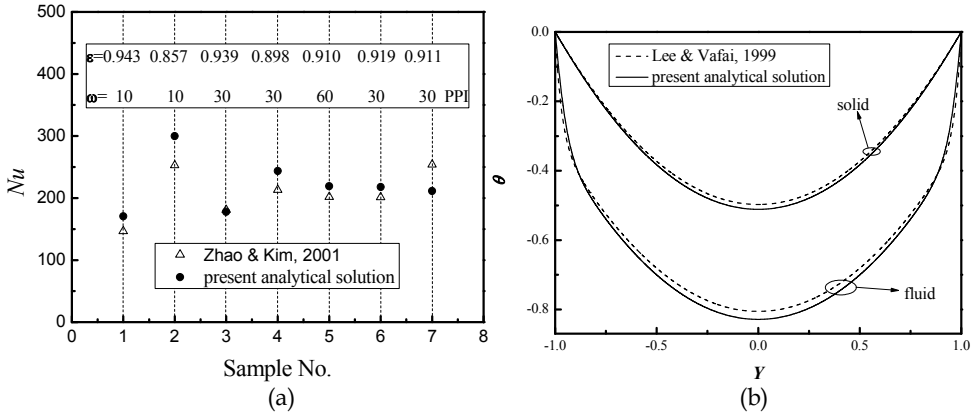

Fig. 7. Validation of present solution: (a) compared with the experiment; (b) compared with Lee and Vafai (Lee & Vafai, 1999) (ε=0.9, ω=10 PPI, H=0.01 m, u_m=1 m/s, k_f/k_s=10^{-4})

Figure 8(a) displays velocity profiles for smooth and metallic foam channels with different porosities and pore densities from the analytical solution for velocity in Eq. (14a). The existence of metallic foams can dramatically homogenize the flow field and velocity gradient near the impermeable wall because the metallic foam channel is considerably higher than that for the smooth channel. With decreasing porosity and increasing pore density, the flow field becomes more uniform and the boundary layer becomes thinner. This implies that high near wall velocity gradient, created by the ability to homogenize flow field for metallic foams, is an important reason for heat transfer enhancement.

Figure 8(b) shows the effect of porosity on the temperature profiles of solid and fluid phases. Porosity has significant influence on both solid and fluid temperatures. When porosity increases, temperature difference between the solid matrix and channel wall is improved. This is because the solid ligament diameter is reduced with increasing porosity under the same pore density, which results in an increased thermal resistance of heat conduction in solid matrix. In addition, the temperature difference between the fluid and channel wall has a similar trend. This is attributed to the reduction of the specific surface

area caused by increasing porosity to create higher heat transfer temperature difference under the same heat transfer rate.

Figure 8(c) illustrates the effect of pore density on temperature profile. It is found that θ_s / k_{se} almost remains unchanged with increasing pore density since effective thermal conductivity and thermal resistance in solid matrix are affected not by pore density but by porosity. While θ_f / k_{se} increases with an increase in pore density, it shows that temperature difference between fluid and solid wall is reduced since the convective thermal resistance is reduced due to the extended surface area.

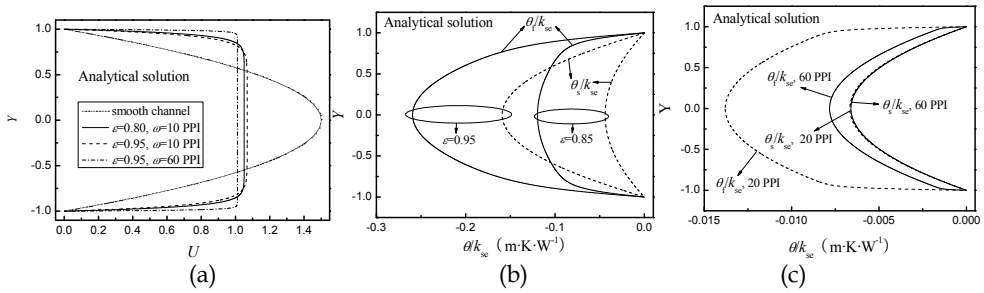

Fig. 8. Effect of metallic foam morphology parameters on velocity and temperature profiles: (a) velocity profile (H=0.005 m); (b) temperature profile affected by porosity (ω=10 PPI, H=0.01 m, u_m=5 m·s^{-1}, k_f/k_s=10^{-4}); (c) temperature profile affected by pore density (ε=0.9, H=0.01 m, u_m=5 m·s^{-1}, k_f/k_s=10^{-5})

3.2.2 Metallic foam partially filled duct

In the second part, fully developed forced convective heat transfer in a parallel-plate channel partially filled with highly porous, open-celled metallic foam is analytically investigated and results proposed by the present author (Xu et al., 2011c) is presented in this section. The Navier-Stokes equation for the hollow region is connected with the Brinkman-Darcy equation in the foam region by the flow coupling conditions at the porous-fluid interface. The energy equation for the hollow region and the two energy equations of solid and fluid for the foam region are linked by the heat transfer coupling conditions. The schematic diagram for the corresponding configuration is shown in Fig. 9. Two isotropic

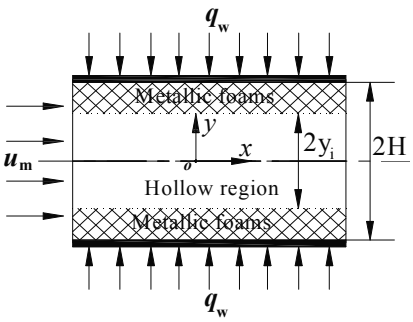

Fig. 9. Schematic diagram of a parallel-plate channel partially filled with metallic foam

and homogeneous metallic foam layers are symmetrically sintered on upper and bottom plates subjected to uniform heat flux. Fluid is assumed to possess constant thermal-physical properties. Thermal dispersion effect is neglected for metallic foams with high solid thermal conductivity (Calmidi & Mahajan 2000). To obtain analytical solution, the inertial term in Eq.(4) is neglected as well.

For the partly porous duct, coupling conditions of flow and heat transfer at the porous-fluid interface can be divided into two types: slip and no-slip conditions. Alazmi and Vafai (Alazmi & Vafai, 2001) reviewed different kinds of interfacial conditions related to velocity and temperature using the one-equation model. It was indicated that the difference between different interfacial conditions for both flow and heat transfer is minimal. However, for heat transfer, since the LTNE model is more suitable for highly conductive metallic foams rather than the LTE model, the implementation of LTNE model on thermal coupling conditions at the foam-fluid interface is considerably more complex in terms of number of temperature variables and number of interfacial conditions compared with LTE model. The momentum equation in the fluid region belongs to the Navier-Stokes equation while that in the foam region is the Brinkman-extended-Darcy equation, which is easily coupled by the flow conditions at foam-fluid interface.

For heat transfer, Ochoa-Tapia and Whitaker (Ochoa-Tapia & Whitaker, 1995) have proposed a series of interface conditions for non-equilibrium conjugate heat transfer at the porous-fluid interface, which can be used for thermal coupling at the foam-fluid interface of a domain party filled with metallic foams. Given that the two sets of governing equations are coupled at the porous-fluid interface, the interfacial coupling conditions must be determined to close the governing equations. Continuities of velocity, shear stress, fluid temperature, and heat flux at the porous-fluid interface should be guaranteed for meaningful physics. The corresponding expressions are shown in Eqs. (18)–(21):

$$u\big|_{y_i^-} = u\big|_{y_i^+} . \tag{18}$$

$$\mu_f \left.\frac{\mathrm{d}u}{\mathrm{d}y}\right|_{y_i^-} = \frac{\mu_f}{\varepsilon} \left.\frac{\mathrm{d}u}{\mathrm{d}y}\right|_{y_i^+} . \tag{19}$$

$$T_f\big|_{y_i^-} = T_f\big|_{y_i^+} . \tag{20}$$

$$k_f \left.\frac{\partial T_f}{\partial y}\right|_{y_i^-} = \left(k_{fe} \frac{\partial T_f}{\partial y} + k_{se} \frac{\partial T_s}{\partial y} \right)\Bigg|_{y_i^+} . \tag{21}$$

There are three variables for two-energy equations: the fluid and solid temperatures of the foam region and the temperature of the open region. Therefore, another coupling condition is required to obtain the temperature of solid and fluid in the foam region (Ochoa-Tapia & Whitaker, 1995), as:

$$k_{se} \nabla T_s\big|_{y_i^+} = h_{sf} \left(T_s\big|_{y_i^+} - T_f\big|_{y_i^-} \right) . \tag{22}$$

For the reason that axial heat conduction can be neglected, Eq. (22) is simplified as follows:

$$k_{\mathrm{se}} \left.\frac{\partial T_{\mathrm{s}}}{\partial y}\right|_{y_{\mathrm{i}}^{+}} = h_{\mathrm{sf}} \left(T_{\mathrm{s}}\big|_{y_{\mathrm{i}}^{+}} - T_{\mathrm{f}}\big|_{y_{\mathrm{i}}^{-}} \right). \tag{23}$$

Due to the fact that the solid ligaments are discontinuous at the foam-fluid interface, heat conduction through the solid phase is totally transferred to the fluid in the manner of convective heat transfer across the foam-fluid interface. Thus, the physical meaning of Eq.(22) stands for the convective heat transfer at the foam-fluid interface from the solid ligament to the fluid nearby. Thus, the governing equations in the foam region and that in the fluid region are linked together via these interfacial coupling conditions.
With the dimensionless qualities in Eqs.(11a)–(11b) and the following variables,

$$Y_i = \frac{y_i}{H}, A = \frac{h_{\mathrm{sf}} H}{k_{\mathrm{se}}}. \tag{24}$$

governing equations for the fluid region and the foam region are normalized. Dimensionless governing equations for the hollow region ($0 \le Y \le Y_{\mathrm{i}}$) are as follows:

$$\frac{\partial^2 U}{\partial Y^2} - \frac{P}{Da} = 0. \tag{25}$$

$$\frac{\partial^2 \theta_{\mathrm{f}}}{\partial Y^2} = \frac{1}{B} U. \tag{26}$$

Dimensionless governing equations for the foam region ($Y_{\mathrm{i}} \le Y \le 1$) are as follows:

$$\frac{\partial^2 U}{\partial Y^2} - s^2 (U + P) = 0. \tag{27}$$

$$\frac{\partial^2 \theta_{\mathrm{s}}}{\partial Y^2} - D(\theta_{\mathrm{s}} - \theta_{\mathrm{f}}) = 0. \tag{28}$$

$$C \frac{\partial^2 \theta_{\mathrm{f}}}{\partial Y^2} + D(\theta_{\mathrm{s}} - \theta_{\mathrm{f}}) = U. \tag{29}$$

Corresponding dimensionless closure conditions are as follows:

$$Y = 0 : \frac{\partial U}{\partial Y} = \frac{\partial \theta_{\mathrm{f}}}{\partial Y} = 0. \tag{30a}$$

$$Y = 1 : U = 0, \theta_{\mathrm{s}} = \theta_{\mathrm{f}} = 0. \tag{30b}$$

When $Y = Y_{\mathrm{i}}$, the dimensionless coupling conditions are as follows:

$$U\big|_{Y_{\mathrm{i}}^{-}} = U\big|_{Y_{\mathrm{i}}^{+}}. \tag{31a}$$

$$\left.\frac{dU}{dY}\right|_{Y_i^-} = \frac{1}{\varepsilon}\left.\frac{dU}{dY}\right|_{Y_i^+} . \tag{31b}$$

$$\theta_f\big|_{Y_i^-} = \theta_f\big|_{Y_i^+} . \tag{31c}$$

$$B\left.\frac{\partial\theta_f}{\partial Y}\right|_{Y_i^-} = \left.\left(C\frac{\partial\theta_f}{\partial Y} + \frac{\partial\theta_s}{\partial Y}\right)\right|_{Y_i^+} . \tag{31d}$$

$$\left.\frac{\partial\theta_s}{\partial Y}\right|_{Y_i^+} = A\left(\theta_s\big|_{Y_i^+} - \theta_f\big|_{Y_i^-}\right). \tag{31e}$$

The velocity field is typically obtained ahead of the temperature field for the uncoupled relationship between the momentum and energy equations. With closure conditions for flow in Eqs. (30a), (30b), (31a), and (31b), the dimensionless velocity equation of Eqs. (25) and (27) can be solved and the solution for velocity is as follows:

$$U = \begin{cases} P\left(\dfrac{1}{2Da}Y^2 + C_0\right), & 0 \le Y \le Y_i \\ P\left(C_1 e^{sY} + C_2 e^{-sY} - 1\right), & Y_i \le Y \le 1 \end{cases} . \tag{32}$$

where dimensionless pressure drop P, constants C_0, C_1, and C_2 are as follows:

$$P = \frac{1}{\dfrac{1}{s}\left(C_1 e^{s} - C_2 e^{-s}\right) + \dfrac{Y_i^3}{6Da} + C_0 Y_i - 1} . \tag{33a}$$

$$C_0 = C_1 e^{sY_i} + C_2 e^{-sY_i} - Y_i^2 / (2Da) - 1 . \tag{33b}$$

$$C_1 = \frac{e^{-sY_i} + sY_i e^{sY_i}}{e^{s(1-Y_i)} + e^{-s(1-Y_i)}} . \tag{33c}$$

$$C_2 = \frac{e^{sY_i} - sY_i e^{s}}{e^{s(1-Y_i)} + e^{-s(1-Y_i)}} . \tag{33d}$$

The solution to the energy equations is as follows:

$$\theta_f = \begin{cases} P\cdot\dfrac{1}{B}\left(\dfrac{1}{24Da}Y^4 + \dfrac{C_0}{2}Y^2 + C_3\right), & 0 \le Y \le Y_i \\ P\left\{\begin{array}{l} C_6 e^{tY} + C_7 e^{-tY} + \dfrac{1 - D/s^2}{C\cdot s^2 - D(C+1)}\left(C_1 e^{sY} + C_2 e^{-sY}\right) \\ -\dfrac{1}{2(C+1)}Y^2 + \dfrac{C_4}{C+1}Y + \dfrac{C_5}{C+1} + \dfrac{1}{D(C+1)^2} \end{array}\right\}, & Y_i \le Y \le 1 \end{cases} . \tag{34a}$$

$$\theta_s = P\begin{Bmatrix} -\frac{1}{C}\left(C_6 e^{tY} + C_7 e^{-tY}\right) - \frac{D/s^2}{C\cdot s^2 - D(C+1)}\left(C_1 e^{sY} + C_2 e^{-sY}\right) \\ -\frac{1}{2(C+1)}Y^2 + \frac{C_4}{C+1}Y + \frac{C_5}{C+1} - \frac{C}{D(C+1)^2} \end{Bmatrix}, \quad Y_i \le Y \le 1 \tag{34b}$$

The constants in the above equation are defined as follows:

$$C_3 = B\begin{bmatrix} C_6 e^{tY_i} + C_7 e^{-tY_i} + \frac{1 - D/s^2}{C\cdot s^2 - D(C+1)}\left(C_1 e^{sY_i} + C_2 e^{-sY_i}\right) \\ -\frac{1}{2(C+1)}Y_i^2 + \frac{C_4}{C+1}Y_i + \frac{C_5}{C+1} + \frac{1}{D(C+1)^2} \end{bmatrix} - \frac{1}{24Da}Y_i^4 - \frac{C_0}{2}Y_i^2 . \tag{35a}$$

$$C_4 = \frac{1}{6Da}Y_i^3 + C_0 Y_i . \tag{35b}$$

$$C_5 = \frac{1}{2} - \frac{1}{s^2} - C_4 . \tag{35c}$$

$$C_6 = \frac{\left[A(C+1) + Ct\right]e^{-tY_i}C_8 - e^{-t}C_9}{\left[A(C+1) + Ct\right]e^{t(1-Y_i)} - \left[A(C+1) - Ct\right]e^{-t(1-Y_i)}} . \tag{35d}$$

$$C_7 = \frac{e^{t}C_9 - \left[A(C+1) - Ct\right]e^{tY_i}C_8}{\left[A(C+1) + Ct\right]e^{t(1-Y_i)} - \left[A(C+1) - Ct\right]e^{-t(1-Y_i)}} . \tag{35e}$$

$$C_8 = -\frac{C\cdot s^2}{D(C+1)^2\left[C\cdot s^2 - D(C+1)\right]} . \tag{35f}$$

$$C_9 = A\left[-\frac{C_1 e^{sY_i} + C_2 e^{-sY_i}}{C\cdot s^2 - D(C+1)} - \frac{1}{D(C+1)}\right] - \frac{C\cdot s^2\cdot Y_i}{(C+1)\left[C\cdot s^2 - D(C+1)\right]} - \frac{C_4}{C+1} . \tag{35g}$$

The bulk dimensionless fluid temperature is expressed as follows:

$$\begin{aligned} \theta_{f,b} &= \frac{\frac{1}{A}\int_A U\theta_f dA}{\frac{1}{A}\int_A U dA} = \int_0^{Y_i} U\theta_f dY + \int_{Y_i}^1 U\theta_f dY = \frac{P^2}{B}\left[\frac{1}{336Da^2}Y_i^7 + \frac{7C_0}{120Da}Y_i^5 + \left(\frac{C_3}{Da} + C_0^2\right)\frac{Y_i^2}{6} + C_0 C_3 Y_i\right] \\ &+ P^2\left\{\frac{C_1C_6}{s+t}\left(e^{(s+t)} - e^{(s+t)Y_i}\right) + \frac{C_1C_7}{s-t}\left(e^{(s-t)} - e^{(s-t)Y_i}\right) - \frac{C_2C_6}{(s-t)}\left(e^{-(s-t)} - e^{-(s-t)Y_i}\right)\right. \\ &- \frac{C_2C_7}{(s+t)}\left(e^{-(s+t)} - e^{-(s+t)Y_i}\right) + \frac{N_1C_1^2}{2s}\left(e^{2s} - e^{2sY_i}\right) - \frac{N_1C_2^2}{2s}\left(e^{-2s} - e^{-2sY_i}\right) + \\ &\frac{C_1}{s}\left[e^{s}\left(N_2 + N_3 - \frac{2N_2}{s} - N_1 + \frac{2N_2}{s^2} - \frac{N_3}{s} + N_4\right) - e^{sY_i}\left(N_2Y_i^2 + \left(N_3 - \frac{2N_2}{s}\right)Y_i - N_1 + \frac{2N_2}{s^2} - \frac{N_3}{s} + N_4\right)\right] - \\ &\frac{C_2}{s}\left[e^{-s}\left(N_2 + N_3 + \frac{2N_2}{s} - N_1 + \frac{2N_2}{s^2} + \frac{N_3}{s} + N_4\right) - e^{-sY_i}\left(N_2Y_i^2 + \left(N_3 + \frac{2N_2}{s}\right)Y_i - N_1 + \frac{2N_2}{s^2} + \frac{N_3}{s} + N_4\right)\right] \\ &\left. - \frac{C_6}{t}\left(e^{t} - e^{tY_i}\right) + \frac{C_7}{t}\left(e^{-t} - e^{-tY_i}\right) - \frac{N_3}{3}\left(1 - Y_i^3\right) - \frac{N_3}{2}\left(1 - Y_i^2\right) + \left(2N_1C_1C_2 - N_4\right)(1 - Y_i)\right\} \end{aligned} \tag{36}$$

In Eq. (36), the constants N_1, N_2, N_3, and N_4 are as follows:

$$N_1 = \frac{1 - D/s^2}{C \cdot s^2 - D(C+1)}, N_2 = -\frac{1}{2(C+1)}, N_3 = \frac{C_4}{C+1}, N_4 = \frac{1}{D(C+1)^2}. \quad (37)$$

Friction factor f and Nusselt number Nu are the same with Eqs. (16a) and (16b).

Velocity profiles predicted by the analytical solutions shown in Eq. (32) at three combinations of porosity and pore density are presented in Fig. 10(a). It is found that velocity in the hollow space is considerably higher than that in the foam region with obstructing foam ligaments. Increasing porosity or decreasing pore density can both increase velocity in foam region and decrease velocity in open region simultaneously since flow resistance in the foam region can be reduced by increasing porosity and decreasing pore density of metallic foams. Figure 10(b) illustrates the comparison of velocity profiles for four hollow ratios: 0 (foam fully filled channel), 0.2, 0.5, 0.8, and 1.0 (smooth channel). The velocity profile is a parabolic distribution for the smooth channel and the profile for fully filled channel is similar, except that the distribution is more uniform since no sudden change of permeability is in the cross section. Comparatively for the foam partially filled channel, sudden change in permeability occurs at the porous-fluid interface; the average velocity in the central fluid region for foam partially filled channel (Y_i=0.2, 0.5, 0.8) is higher than those of the foam fully filled channel and empty channel. Moreover, maximum velocity in the central region decreases with the increase in hollow ratio due to the sizeable difference in permeability between porous and clear fluid regions. Velocity in the foam region of foam partially filled channel is considerably lower than those of foam fully filled channel and smooth channel.

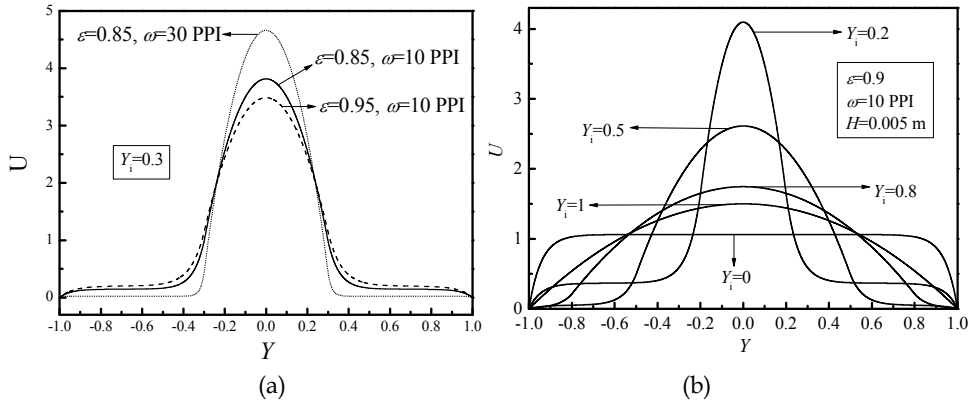

(a) (b)

Fig. 10. Effect of key parameters on velocity profiles: (a) metal foam morphology parameters; (b) hollow ratio

Figure 11(a) presents the influence of porosity on temperature profile. Evidently, the nominal excess temperature of fluid in the hollow region decreases in the y direction and the decreasing trend becomes less obvious in the foam region. This is due to the total thermal resistance in the foam region, which is lower than that in the hollow region for the significant heat transfer surface extension. The nominal excess temperatures of fluid and

solid in the foam region for ε =0.9 were lower than that for ε =0.95 because decreased porosity leads to the increase in both the effective thermal conductivity and the foam surface area to improve the corresponding heat transfer with the same heat flux. Effect of pore density on temperature profile is shown in Fig. 11(b). The solid excess temperature is almost the same in the foam region for different pore densities. This is attributed mainly to the effect of porosity on heat conduction thermal resistance of the foam, as shown in Table 1. On the other hand, the nominal excess fluid temperature of 5 PPI is significantly smaller than that of 30 PPI. The trend inconsistency of the fluid and solid temperatures in the two regions for the two pore densities is caused by mass flow fraction in the foam region. The local convective heat transfer coefficient for 5 PPI was higher than 30 PPI due to the relative higher mass flow fraction in the foam region.

However, the heat transfer surface area inside the foam of 5 PPI is lower than that of 30 PPI. The two opposite effects competed with each other, resulting in the identical temperature difference between wall and fluid in the foam region. However, in the hollow region, the porous-fluid interface area becomes the only surface area where porosity for the two pore densities is the same. Hence, the temperature difference between wall and fluid for 5 PPI is reduced and obviously lower than that for 30 PPI.

Figure 11(c) presents the comparison between fluid and solid temperature distribution for different channels, including empty channel (Y_i=1), foam partially filled channel (Y_i=0.5), and foam fully filled channel (Y_i=0). The nominal excess temperature becomes dependent on the heat transfer area and local heat transfer coefficient. In the hollow region, the heat transfer surface area is reduced to the interface area for the foam partially filled channel (Y_i=0.5), which was considerably smaller than the volume surface area of the fully filled channel (Y_i=0). The nominal fluid excess temperature increases in the order of Y_i=1, Y_i=0.5, and Y_i=0 since the total convective thermal resistance $1/(h_{sf}a_{sf})$ decreases in the order Y_i=0, Y_i=0.5, Y_i=1 in the clear fluid region. In the near-wall foam region, local heat transfer coefficient for Y_i=0.5 is reduced compared with that for Y_i=0. However, the effect of fluid heat conduction dominates in the near-wall area, resulting in a lower nominal fluid excess temperature for Y_i=0.5 compared with that for the foam fully filled channel (Y_i=0). Thus, an intersection point occurs in the curve of the fluid excess temperature distribution.

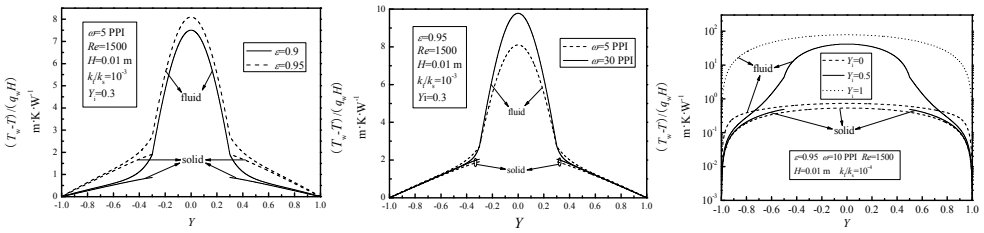

(a) (b) (c)

Fig. 11. Effects of key parameters on temperature profiles: (a) porosity; (b) pore density; (c) hollow ratio

Figure 12(a) presents the effect of porosity on *Nu* for four different metal materials: steel, nickel, aluminum, and copper with air as working fluid. The Nusselt number does not

monotonically increase with porosity increase and a maximum value of *Nu* exists at a critical porosity. This can be attributed to the fact that increasing porosity will lead to a decrease in effective thermal conductivity and an increase in mass flow rate in the foam region. Below the critical porosity, the increase in the mass flow region prevails and *Nu* increases to the maximum value. When porosity is higher than the critical value, which approaches 1, the decrease in thermal conductivity prevails. The Nusselt number sharply reduces and approaches the value of the smooth channel.

It is observed that the increase in the solid thermal conductivity can result in an increase in *Nu*. The critical porosity likewise increases with the solid thermal conductivity. It is implied that porosity should be maintained at an optimal value in the design of related heat transfer devices to maximize the heat transfer coefficient. Figure 12(b) shows the effect of pore density on *Nu* for different hollow ratios in which the two limiting cases for Y_i =1 (J.H. Lienhard IV & J.H. Lienhard V, 2006) and Y_i=0 (Mahjoob & Vafai, 2009) are compared as references. As Y_i approaches 1, the predicted *Nu* of the present analytical solution, with a value of 8.235, coincides accurately with that of the smooth channel (J.H. Lienhard IV & J.H. Lienhard V, 2006). As Y_i approaches 0, the difference between the present analytical result and that of Mahjoob and Vafai (Mahjoob & Vafai, 2009) is very mild since the effect of viscous force of impermeable wall is considered in the present work and not considered in the research of Mahjoob and Vafai (Mahjoob & Vafai, 2009) with the Darcy model. This provides another evidence for feasibility of present analytical solution.

Moreover, it is found that the Nusselt number gradually decreases to a constant value as pore density increases. Increasing pore density can improve the heat transfer surface area but lead to drastic reduction in mass flow rate in the foam region. Hence, small pore density is recommended to maintain heat transfer performance and to reduce pressure drop for thermal design of related applications. The effect of hollow ratio on *Nu* under various k_f/k_s is shown in Fig. 12(c). At high k_f/k_s (1, 10^{-1}), a minimized *Nu* exists as Y_i varies from 0 to 1, which is in accordance with the thermal equilibrium result of Poulikakos and Kazmierczak (Poulikakos & Kazmierczak, 1987). However, *Nu* monotonically decreases as Y_i varies from 0 to 1 for low k_f/k_s, as in the case of metallic foams with high solid thermal conductivities. This is attributed to the fact that both the mass flow rate and foam surface area in the foam region are reduced as Y_i increases. As Y_i approaches 1, the Nusselt number gradually converges to the value 8.235, which is the exact value of forced convective heat transfer in the smooth channel (Y_i=1).

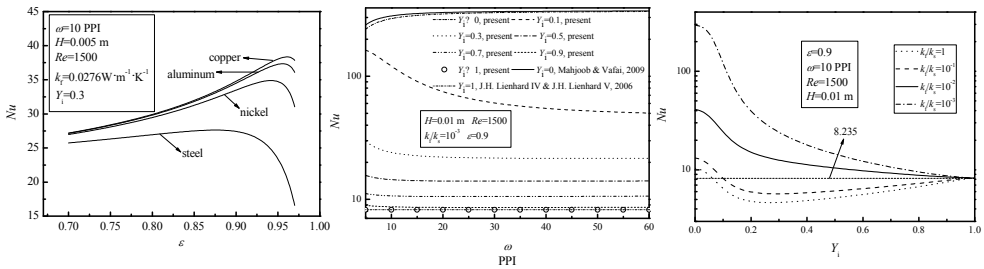

(a) (b) (c)

Fig. 12. Effects of key parameters on Nu: (a) porosity; (b) pore density; (c) hollow ratio

3.3 Numerical modeling for double-pipe heat exchangers

In this section, the two-energy-equation numerical model has been applied to parallel flow double-pipe heat exchanger filled with open-cell metallic foams. The numerical results of the present authors (Du et al., 2010) are introduced in this section. In the model, the solid-fluid conjugated heat transfer process with coupling heat conduction and convection in the open-celled metallic foam, interface wall, and clear fluid in both inner and annular space in heat exchanger is fully considered. The non-Darcy effect, thermal dispersion (Zhao et al., 2001), and wall thickness are taken into account as well.

Figure 13 shows the schematic diagram of metal foam filled double-pipe heat exchanger with parallel flow, in which the cylindrical coordinate system and adiabatic boundary condition in the outer surface of the annular duct are shown. The interface-wall with thickness δ is treated as conductive solid block in the internal part of metallic foams. R_1, R_2, and R_3 represent the inner radius of the inner pipe, outer radius of the inner pipe, and inner radius of the outer pipe, respectively. Fully developed conditions of the velocity and temperature at the exit are adopted. For simplification, incompressible fluids with constant physical properties are considered. Metallic foams are isotropic, possessing no contact resistance on the interface wall.

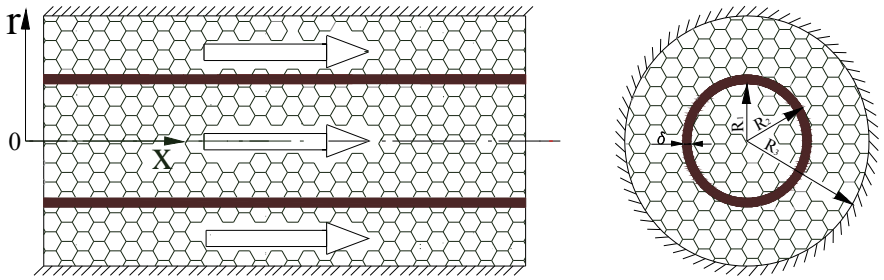

Fig. 13. Schematic diagram of double-pipe heat exchanger with parallel flow

With the Forchheimer flow model for momentum equation and two-equation model for energy equations, the flow and heat transfer problem shown in Fig. 13 is described with the following governing equations:

Continuity equation:

$$\frac{\partial(\rho_f u)}{\partial x}+\frac{1}{r}\frac{\partial(r\rho_f v)}{\partial r}=0\,. \tag{38}$$

Momentum equations:

$$\frac{\partial(\rho_f u^2)}{\partial x}+\frac{1}{r}\frac{\partial(r\rho_f uv)}{\partial r}=-\varepsilon^2\frac{\partial p}{\partial x}+\frac{\partial}{\partial x}(\mu_f\varepsilon\frac{\partial u}{\partial x})+\frac{1}{r}\frac{\partial}{\partial r}(r\mu_f\varepsilon\frac{\partial u}{\partial r})-\frac{\mu_f\varepsilon^2}{K}u-\frac{\rho_f\varepsilon^2 C_I u^2}{\sqrt{K}}\,. \tag{39a}$$

$$\frac{\partial(\rho_f uv)}{\partial x}+\frac{1}{r}\frac{\partial(r\rho_f v^2)}{\partial r}=-\varepsilon^2\frac{\partial p}{\partial r}+\frac{\partial}{\partial x}(\mu_f\varepsilon\frac{\partial v}{\partial x})+\frac{1}{r}\frac{\partial}{\partial r}(r\mu_f\varepsilon\frac{\partial v}{\partial r})-\frac{\mu_f\varepsilon^2}{K}v-\frac{\rho_f\varepsilon^2 C_I v^2}{\sqrt{K}}\,. \tag{39b}$$

Two energy equations:

$$\frac{\partial}{\partial x}\left(k_{\mathrm{se}}\frac{\partial T_{\mathrm{s}}}{\partial x}\right)+\frac{1}{r}\frac{\partial}{\partial r}\left(rk_{\mathrm{se}}\frac{\partial T_{\mathrm{s}}}{\partial r}\right)-h_{\mathrm{sf}}a_{\mathrm{sf}}(T_{\mathrm{s}}-T_{\mathrm{f}})=0\,. \tag{40a}$$

$$\frac{\partial(\rho_{\mathrm{f}}uT_{\mathrm{f}})}{\partial x}+\frac{1}{r}\frac{\partial(r\rho_{\mathrm{f}}vT_{\mathrm{f}})}{\partial r}=\frac{\partial}{\partial x}\left(\frac{k_{\mathrm{fe}}+k_{\mathrm{d}}}{c_{\mathrm{f}}}\frac{\partial T_{\mathrm{f}}}{\partial x}\right)+\frac{1}{r}\frac{\partial}{\partial r}\left(r\frac{k_{\mathrm{fe}}+k_{\mathrm{d}}}{c_{\mathrm{f}}}\frac{\partial T_{\mathrm{f}}}{\partial r}\right)+\frac{h_{\mathrm{sf}}a_{\mathrm{sf}}}{c_{\mathrm{f}}}(T_{\mathrm{s}}-T_{\mathrm{f}})\,. \tag{40b}$$

where x and r pertain to cylindrical coordinate system. The tortuous characteristic of fluids in metallic foams enhances heat transfer coefficients between fluid and solid, influence of which is considered by introducing dispersion conductivity k_{d} (Zhao et al., 2001).

In the interfacial wall domain, the conventional two-equation model cannot be directly used since no fluid can flow through the wall. Hence, particular treatments are proposed to take into account the interface wall. Special fluids can be assumed to exist in the interface wall such that the fluid-phase equation in Eq. (40b) can be applied. However, the dispersion conductivity k_{d} is considered to be zero and the viscosity of fluid can be considered to be infinite, thus leading to zero fluid velocity. As such, the temperature and efficient thermal conductivity of the special fluid and solid are the same, that is to say, $T_{\mathrm{s}}=T_{\mathrm{f}}$, $k_{\mathrm{fe}}=k_{\mathrm{se}}$. In this condition, Eqs. (40a) and (40b) are unified into one for the interface wall, as seen in Eq. (41):

$$\frac{\partial}{\partial x}\left(k_{\mathrm{se}}\frac{\partial T_{\mathrm{s}}}{\partial x}\right)+\frac{1}{r}\frac{\partial}{\partial r}\left(rk_{\mathrm{se}}\frac{\partial T_{\mathrm{s}}}{\partial r}\right)=0\,. \tag{41}$$

According to this extension, the temperature and wall heat flux distribution can be determined by Eq. (43a) during the iteration process, instead of being described as a constant value in advance. Due to the continuity of the interfacial wall heat flux, the inner side wall heat flux q_{inner} and the annular side wall heat flux q_{annular} are formulated in Eq. (42).

$$q_{\mathrm{inner}}=-q_{\mathrm{annular}}\frac{R_2}{R_1}\neq 0\,. \tag{42}$$

where q is the heat flux and the subscripts 'inner' and 'annular' respectively denotes physical qualities relevant to the inner-pipe and the annular space. Simultaneously heat transfer through solid and fluid at the wall can be obtained using the method formulated by Lu and Zhao et al. (Lu et al., 2006; Zhao et al., 2006), which is frequently used and validated in relevant research. The two heat fluxes are expressed as:

$$q_{\mathrm{inner}}=\left(k_{\mathrm{se}}\frac{\partial T_{\mathrm{s}}}{\partial r}+k_{\mathrm{fe}}\frac{\partial T_{\mathrm{f}}}{\partial r}\right)\Bigg|_{r=R_1}\quad\text{(inner side)} \tag{43a}$$

$$q_{\mathrm{annular}}=-\left(k_{\mathrm{se}}\frac{\partial T_{\mathrm{s}}}{\partial r}+k_{\mathrm{fe}}\frac{\partial T_{\mathrm{f}}}{\partial r}\right)\Bigg|_{r=R_2}\quad\text{(annular side)} \tag{43b}$$

Conjugated heat transfer between heat conduction in the interfacial wall and metal ligament, as well as the convection in the fluid, are solved within the entire computational domain.

On the center line of the double-pipe heat exchanger, symmetric conditions are adopted. No-slip velocity and adiabatic thermal boundary conditions for the outside wall of the heat exchanger are conducted as well. Since the wall is adiabatic, the heat flux equals to zero when temperatures of the fluid and solid matrices are equivalent. At the entrance of the double pipe, velocities and fluid temperatures in both flow passages are given as uniform distribution profiles, while the gradient of the metallic foam temperature is equal to zero, according to Lu and Zhao et al. (Lu et al., 2006; Zhao et al., 2006). Fully developed conditions are adopted at the outlet. For the interface wall, velocity of the fluid is zero, as previously determined, which indicates that dynamic viscosity is infinite. The specifications of the boundary conditions are shown in Table 2. Both governing equations are described using the volume-averaging method. During code development, the two equations are unified over the entire computational domain. The above special numerical treatment is implemented in the wall domain.

	x-velocity u	y-velocity v	Fluid temperature T_f	Solid temperature T_s
$x=0$	$u=u_{in}$	$v=0$	$T_f=T_{f,in}$	$\frac{\partial T_s}{\partial x}=0$
$x=L$	$\frac{\partial u}{\partial x}=0$	$\frac{\partial v}{\partial x}=0$	$\frac{\partial T_f}{\partial x}=0$	$\frac{\partial T_s}{\partial x}=0$
$r=0$	$\frac{\partial u}{\partial r}=0$	$v=0$	$\frac{\partial T_f}{\partial r}=0$	$\frac{\partial T_s}{\partial r}=0$
$R_1 \le r \le R_2$	$u=0$	$v=0$	$T_s=T_f$	$T_s=T_f$
$r=R_3$	$u=0$	$v=0$	$q=k_{fe}\frac{\partial T_f}{\partial r}+k_{se}\frac{\partial T_s}{\partial r}=0$, $T_s=T_f$	

Table 2. Boundary conditions for numerical simulation of double-pipe heat exchanger

The simulation is performed according to the volume-averaging method, based on the geometrical model of open-cell metallic foams provided by Lu et al. (Lu et al., 2006). The codes are validated by comparison with Lu and Zhao et al. (Lu et al., 2006; Zhao et al., 2006). The criterion for ceasing iterations is a relative error of temperatures less than 10^{-5}. The thermo-physical properties of fluid and important parameters in the numerical simulation are shown in Table 3.

To monitor vividly the temperature distribution along the flow direction, a dimensionless temperature is defined as follows:

$$\theta_s=\frac{T_s-T_s\big|_{r=R_2}}{T_{s,b}-T_s\big|_{r=R_2}}. \tag{44a}$$

$$\theta_f=\frac{T_f-T_s\big|_{r=R_2}}{T_{f,b}-T_s\big|_{r=R_2}}. \tag{44b}$$

where $T_{s,b}$ and $T_{f,b}$ represent the cross-sectional bulk mean temperature of solid matrix and fluid phase, respectively, defined as follows:

Parameter	Unit	Value
Reynolds number *Re*	1	3329
Prandtl number *Pr*	1	0.73
Density of inner fluid ρ_{inner}	$\text{kg}\cdot\text{m}^{-3}$	1.13
Density of annular fluid ρ_{annular}	$\text{kg}\cdot\text{m}^{-3}$	1.00
Thermal conductivity of inner fluid $k_{\text{f,inner}}$	$\text{W}\cdot\text{m}^{-1}\cdot\text{K}^{-1}$	0.0276
Thermal conductivity of annular fluid $k_{f,annular}$	$\text{W}\cdot\text{m}^{-1}\cdot\text{K}^{-1}$	0.0305
Kinematic viscousity of inner fluid $\mu_{\text{f,inner}}$	$\text{Pa}\cdot\text{S}$	1.91×10^{-5}
Kinematic viscousity of annular fluid $\mu_{\text{f,annular}}$	$\text{Pa}\cdot\text{S}$	2.11×10^{-5}
Solid thermal conductivity k_{s}	$\text{W}\cdot\text{m}^{-1}\cdot\text{K}^{-1}$	100
Heat capacity at constant pressure of inner fluid $c_{\text{p,inner}}$	$\text{J}\cdot\text{kg}^{-1}\cdot\text{K}^{-1}$	1005
Inlet temperature of inner fluid $T_{\text{in,1}}$	$^{\text{o}}\text{C}$	38
Inlet temperature of annular fluid $T_{\text{in,2}}$	$^{\text{o}}\text{C}$	78

Table 3. Fluid flow and metal foam parameters of the double-pipe heat exchanger

$$T_{\text{f,b}}=\frac{\int_0^{R_1}u\cdot T_{\text{f}}\cdot r\cdot \text{d}r}{\int_0^{R_1}u\cdot r\cdot \text{d}r},\quad T_{\text{s,b}}=\frac{2}{{R_1}^2}\int_0^{R_1}T_{\text{s}}\cdot r\cdot \text{d}r \text{ (inner side)} \tag{45a}$$

$$T_{\text{f,b}}=\frac{\int_{R_2}^{R_3}u\cdot T_{\text{f}}\cdot r\cdot \text{d}r}{\int_{R_2}^{R_3}u\cdot r\cdot \text{d}r},\ T_{\text{s,b}}=\frac{2}{{R_3}^2-{R_2}^2}\int_{R_2}^{R_3}T_{\text{s}}\cdot r\cdot \text{d}r \text{ (annular side)} \tag{45b}$$

The Reynolds number for the inner and annular sides is defined as follows:

$$Re=\frac{\rho u_{\text{m}}D_{\text{h}}}{\mu_{\text{f}}}. \tag{46}$$

where D_{h} is the hydraulic diameter equaling $2R_1$ for the inner side and $2(R_3\text{-}R_2)$ for the annular side. The Nusselt number at the inner and annular sides is defined as follows:

$$Nu=\frac{hD_{\text{h}}}{k_{\text{f}}}. \tag{47}$$

where h is the average convective heat transfer coefficient defined in Eq. (21) for the entire double-pipe heat exchanger for each space.

$$h=\frac{\int_0^L h_{\text{x}}(T_{\text{w,x}}-T_{\text{b,x}})\pi 2R_1\text{d}x}{A_{\text{inner}}\left(T_{\text{w,av}}-T_{\text{f,b}}\right)}=\frac{\int_0^L q_{\text{x}}\text{d}x}{L\left(T_{\text{w,av}}-T_{\text{f,b}}\right)}. \tag{48a}$$

$$h_x = \frac{q_x}{T_{w,x} - T_{f,b,x}}. \tag{48b}$$

where $\boldsymbol{T}_{w,av}$ is the average interface wall temperature and $\boldsymbol{T}_{f,b}$ is the mean fluid temperature, which are defined in Eqs.(22) and (23) for both sides.

$$T_{f,inner} = \frac{T_{in,1} + T_{out,1}}{2} \text{ (for inner space)} \tag{49a}$$

$$T_{f,annular} = \frac{T_{in,2} + T_{out,2}}{2} \text{ (for annular side space)} \tag{49b}$$

The overall heat transfer coefficient $\boldsymbol{U}$ is defined as follows:

$$U = \frac{c_{inner}\rho_{inner}u_{inner}R_1\left(T_{out,1} - T_{in,1}\right)}{8L(T_{f,annlular} - T_{f,inner})}. \tag{50}$$

Figure 14 shows the fluid temperature distribution along the axial direction in the inner-pipe and the annulus for smooth double-pipe HEX (heat exchanger) and metal foam fully filled HEX in condition of ε =0.9, 20 PPI, Re_{inner}=$Re_{annular}$=3329. It is found that $\partial\theta_f / \partial x = 0$ holds in hollow heat exchanger when L/D>125, which has critical value $L/2R_1$≈0.05 $RePr$=121 for fully developed flow region of empty channel. However, the ratio of length to inner diameter for the entrance zone for foam filled heat exchanger is extended to approximately 180 because the foam creates redistribution of the flow profile and enlarges the length of entrance region. Hence, predicted results at axial location ($L/2R_1$=200) could be compared with previous results (Lu et al., 2006; Zhao et al., 2006), which are suitable for fully developed regions.

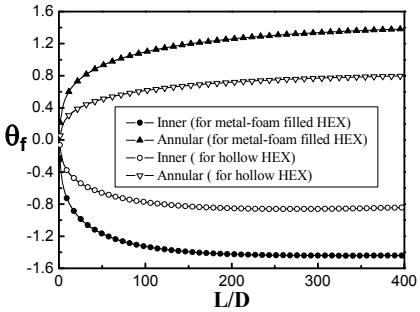

Fig. 14. Predicted dimensionless temperature distribution along the axial direction (for metallic foams ε =0.9, 20PPI, Re_{inner}=$Re_{annular}$=3329)

Interface wall heat flux distribution along axial direction could be further predicted by the coupling interface wall and fluids in two sides. Interface wall heat flux is gained with

$$q_x = k_s \frac{T_{r=R_2} - T_{r=R_2}}{\delta}. \tag{51}$$

The interface wall heat flux distributions and local heat transfer coefficients for metal foam filled double-pipe and hollow double-pipe heat exchangers are shown in Fig. 15. The interface wall heat flux decreased significantly from the inlet to the outlet, as shown in Fig. 15(a). The heat flux at the inlet location is approximately 4.5 times that at the outlet location, while previous models neglect this variation trend. The predicted average interface wall heat flux in the case of exchangers filled with metallic foams is a little lower than the case without foams due to the significant extension of surface area. The local heat transfer coefficient for metallic foam filled double-pipe exchangers is considerably higher than the air flow across the smooth plate from the analytical solution (Incropera et al., 1985), which is attributed to the increased specific surface area by metallic foams, as seen in Fig. 15(b).

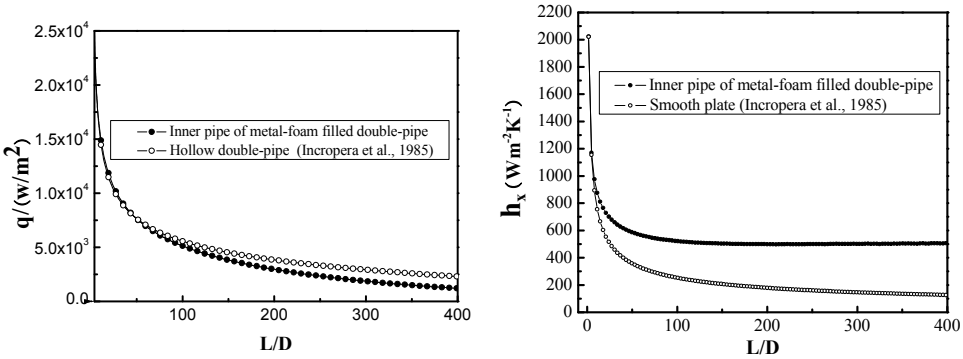

Fig. 15. Predicted interface wall heat flux and local heat transfer coefficient along axial direction (ε =0.9, 20PPI, Re_{inner}=$Re_{annular}$=3329): (a) Local heat flux; (b) Local heat transfer coefficient

Figure 16 displays the influence of metallic foam porosity on the dimensionless fluid and solid temperatures in the radial direction under the same pore density (20 PPI). Figure 16(a)

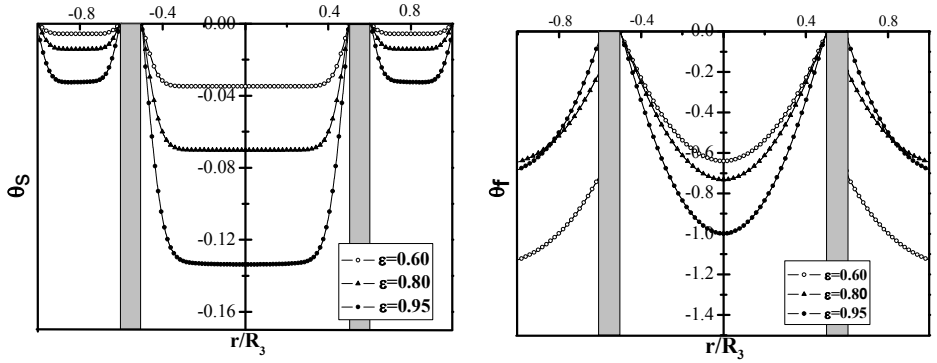

Fig. 16. Effect of porosity on dimensionless temperature distribution (ε =0.9, 20 PPI, Re_{inner}=$Re_{annular}$=3329): (a) Solid temperature; (b) Fluid temperature

shows that with increasing porosity, the dimensionless solid foam matrix temperature increases, and the temperature difference between the matrix and interface wall is improved. This is attributed to reductions in the porous ligament diameter with increasing porosity under the same pore density, leading to increased thermal resistance of heat conduction. The influence of porosity on dimensionless fluid temperatures is more complicated due to conjugated heat transfer, as shown in Fig. 16(b). With increase in porosity, the dimensionless fluid temperature increases in the inner tube, but decreases in the annular space.

Figure 17 displays the effects of pore density and porosity of metallic foams on overall heat-transfer performance. The predicted value is lower than that in the conventional model, shown in Figs. 17(a) and 17(b) since the conventional uniform heat flux model is an ideal case for amplifying the thermal performance of the heat exchanger to over-evaluate the overall heat transfer coefficient. It is indicated that the heat transfer performance is enhanced by increasing the pore density due to increasing heat transfer surface area; it is weakened by increasing porosity due to decreasing diameter of cell ligament.

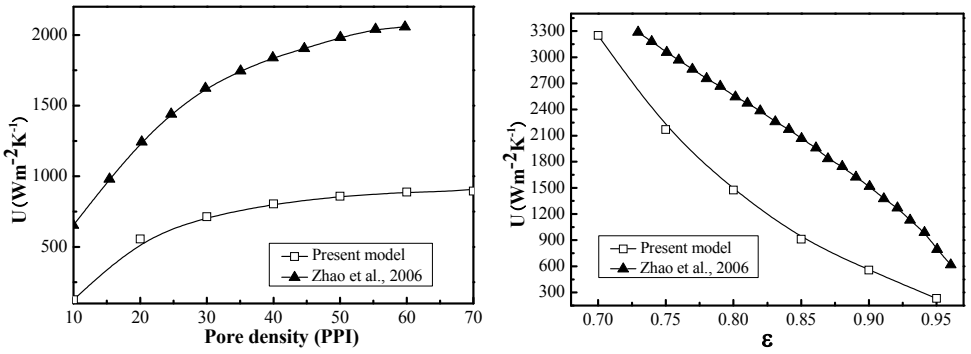

Fig. 17. Effects of metal-foam parameters on overall heat transfer: (a) Pore density; (b) Porosity

4. Condensation on surface sintered with metallic foams

In this section, numerical modeling of film condensation on the vertical wall embedded in metallic foam of the present authors (Du et al., 2011) is presented. In the model, the advection and inertial force in the condensate film are thoroughly considered, from which the non-linear effect of cross-sectional temperature distribution on the condensation heat transfer is involved as well.

Due to substantial heat transferred from saturated vapor to super-cold solid wall, the condensation phenomenon extensively exists in nature, human activities, and industrial applications, such as dew formation in the morning, frost formation on the window in the cold winter, condensation from refrigerant vapor in air-conditioning, water-cooled wall in boiler, and so on. In principle, condensation can be classified into film-wise condensation and drop-wise condensation. However, most condensation phenomena are film-wise form

for the reason that drop-wise condensation is difficult to produce and that it will not last in the face of generation of liquid drops adhered on the solid surface.

Film-wise condensation, likewise called film condensation, was first analytically treated by Nusselt as early as 1916 by introducing the Nusselt theory (Nusselt, 1916). Similar extensive works or experimental studies of film condensation were performed extensively (Dhir & Lienhard, 1971; Popiel & Boguslawski, 1975; Sukhatme et al., 1990; Cheng & Tao, 1994). The use of porous structure for extensive surface of condensation was not a new idea and numerous related studies were found in open literature (Jain & Bankoff, 1964; Cheng & Chui, 1984; Masoud et al., 2000; Wang & Chen et al., 2003; Wang & Yang et al., 2003; Chang, 2008). Metallic foams possess a three-dimensional basic cell geometry of tetrakaidecahedron with specific surface area as high as 10^3-10^4 $m^2 \cdot m^{-3}$. This provides a kind of ideal extended surface for condensation heat transfer. This attractive metallic porous structure motivates the present authors to perform related research on condensation heat transfer, which is shown below.

Overall, the physical process for film condensation is a thickening process of liquid film. The present authors aim to explore condensation mechanisms on surfaces covered with metallic foams and establish a numerical model for film condensation heat transfer within metallic foams, in which the non-linear temperature distribution in the condensation layer was solved. The characteristics of condensation on the vertical plate embedded in metallic foams were discussed and compared with those on the smooth plate.

The schematic diagram for the problem discussed is shown in Fig. 18 with the coordinate system and boundary conditions for the computational domain denoted. Dry saturated vapor of water at atmospheric pressure is static near the vertical plate covered with metallic foams. Due to gravity, condensate fluid flows downward along the plate. Width and length of the computational domain are 5×10^{-4} m and 1 m, respectively. Flow direction of condensing water is denoted by x while thickness direction is denoted by y. The positive x direction is the direction of gravity as well. The temperature of the plate is below the saturated temperature of the vapor, allowing condensation to take place favorably.

Effects of wall conduction and forced convection of the saturated gas are neglected due to the condition of unchanged temperature and zero velocity, respectively. Because of the complexity of the tortuous characteristic of fluid flow in metallic foams, laminar film condensation is assumed for simplification. The metallic foams are assumed to be both isotropic and homogeneous. The fluid is considered to be incompressible with constant properties. Thermal radiation is ignored. Thermal dispersion effect is neglected. The quadratic term for high-speed flow in porous medium are neglected as well for momentum equation in the present study.

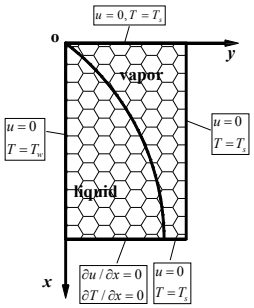

Fig. 18. Computational domain and boundary conditions

Based on the Nusselt theory, vapor density, shear stress on the interface, convection, and inertial force in the condensate layer are all considered. The Darcy model with local thermal equilibrium is adopted to establish the momentum equation. To condensate film of water within the range of $x \geq 0$, $0 \leq y \leq \delta(x)$, the momentum equation is as follows:

$$\frac{\mu}{\varepsilon}\frac{\partial^2 u_l}{\partial y^2} - \frac{\mu}{K}u_l + g(\rho_l - \rho_v) = 0 . \tag{52}$$

where K, g pertain to the permeability of metallic foams and acceleration of gravity, respectively, and u_l, ρ_l, ρ_v denote liquid velocity, liquid density, and vapor density, respectively. Based on the liquid velocity distribution, liquid mass flux at a certain location is shown as follows:

$$q_m = \int_0^{\delta(x)} \rho u_l dy . \tag{53}$$

For the energy equation, the convective term is partially considered since the span wise is assumed to be zero based on the Nusselt theory. Hence, the energy equation is expressed as:

$$u_l \frac{\partial T_l}{\partial x} = \frac{k_{e,l}}{\rho_l c_l}\frac{\partial^2 T_l}{\partial y^2} . \tag{54}$$

where $\boldsymbol{k}_{e,l}$ is the effective thermal conductivity of metallic foams saturated with liquid and referred from Boomsma and Poulikakos (Boomsma & Poulikakos, 2002), while $\boldsymbol{u}_l$, $\boldsymbol{T}_l$ pertain to vapor velocity and liquid temperature, respectively. In the vertical wall for liquid film, heat transfers through phase change of saturated vapor are equal to the heat condition through the vertical wall along the thickness direction of the condensate layer.

$$r \cdot \mathrm{d}q_m = k_l \cdot \left.\frac{\partial T_l}{\partial y}\right|_{y=0} \cdot \mathrm{d}x . \tag{55}$$

where $\boldsymbol{r}$, $\boldsymbol{k}_l$ denote the latent heat of saturated water, conductivity of liquid water, and thickness of the condensate layer, respectively. $\boldsymbol{T}_s$, $\boldsymbol{T}_w$ pertain to saturated temperature and wall temperature, respectively. $\mathrm{d}\boldsymbol{q}_m$ is the differential form of liquid film mass flux.

For convenience of numerical implementation, a square domain is selected as computational domain. Boundary conditions of governing equations in the whole computational domain for Eqs. (52) and (54) are shown in Fig. 18. By iterative methods, the thickness of the condensate layer is obtained with Eq. (52)-(55). The inner conditions at the liquid-vapor interface are set by considering the shear stress continuity as follows:

$$y = 0, \quad u = 0 \quad T = T_w . \tag{56a}$$

$$y = \delta(x), \quad \frac{\partial u_l}{\partial y} = 0 \quad T = T_s . \tag{56b}$$

Certain parameters used are defined below. The Jacobi number is defined as follows:

$$Ja = \frac{r}{c_l \cdot (T_s - T_w)} . \tag{57}$$

The local heat transfer coefficient and Nusselt number along the x direction can be obtained in Eqs. (59) and (60):

$$h(x) = \frac{k_e}{T_w - T_s} \frac{\partial T_l}{\partial y}\bigg|_{y=0} = \frac{1}{\delta(x)} \frac{k_e}{T_w - T_s} \frac{\partial T_l}{\partial [y / \delta(x)]}\bigg|_{y=0} . \tag{58}$$

$$Nu(x) = h(x) \frac{x}{k_e} . \tag{59}$$

The condensate film Reynolds number is expressed as follows:

$$Re(x) = \frac{4h(x)}{c_l \cdot Ja \cdot \mu_l} . \tag{60}$$

In the region outside condensation layer, the domain extension method is employed, where special numerical treatment is implemented during the inner iteration to ensure that velocity and temperature in this extra region are set to be zero and T_s, and that these values cannot affect the solution of velocity and temperature field inside condensation layer.
The governing equations in Eqs. (52)-(54) are solved with using SIMPLE algorithm (Tao, 2005). The convective terms are discritized using the power law scheme. A 200×20 grid system has been checked to gain a grid independent solution. The velocity field is solved ahead of the temperature field and energy balance equation. By coupling Eqs. (52)-(55), the non-linear temperature field can be obtained. The thermal-physical properties in the numerical simulation, involving the fluid thermal conductivity, fluid viscosity, fluid specific heat, fluid density, fluid saturation temperature, fluid latent heat of vaporization, and gravity acceleration are presented in Table 4.

Parameter	Unit	Value
Liquid density ρ_l	$kg \cdot m^{-3}$	977.8
Vapor density ρ_v	$kg \cdot m^{-3}$	0.58
Liquid kinematic viscousity μ_l	$Pa \cdot s$	2.825×10^{-4}
Liquid thermal conductivity k_l	$W \cdot m^{-1} \cdot K^{-1}$	0.683
Liquid heat capacity at constant pressure c_l	$J \cdot kg^{-1} \cdot K^{-1}$	4200
Saturation temperature T_s	°C	100
Latent heat r	$J \cdot kg^{-1}$	297030
Gravity acceleration g	$m \cdot s^{-2}$	9.8

Table 4. Constant parameters in numerical procedure of film condensation

For a limited case of porosity being equal to 1, the present numerical model can predict film condensation on the vertical smooth plate for reference case validation. The distribution of film condensate thickness and local heat transfer coefficient on the smooth plate predicted by the present numerical model with those of Nusselt (Nusselt, 1916) and Al-Nimer and Al-Kam (Al-Nimer and Al-Kam, 1997) are shown in Fig. 19. It can be seen that the numerical solution is approximately consistent with either Nusselt (Nusselt, 1916) or Al-Nimer and Al-Kam (Al-Nimer and Al-Kam, 1997). The maximum deviation for condensate thickness and local heat transfer coefficient is 14.5% and 12.1%, respectively.

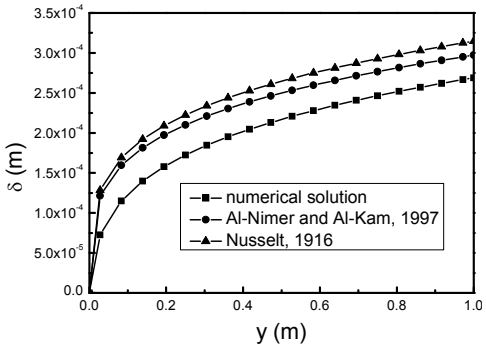

Fig. 19. Distribution of condensate thickness for the smooth plate (ε =0.9, 10 PPI)

Figure 20(a) exhibits the temperature distribution in condensate layer for three locations in the vertical direction (x/L=0.25, 0.5, and 0.75) with porosity and pore density being 0.9 and 10 PPI, respectively. Evidently, the temperature profile is nonlinear. The non-linear characteristic is more significant, or the defined temperature gradient $\partial T_l / \partial\left[y / \delta(x)\right]$ is higher in the downstream of condensate layer since the effect of heat conduction thermal resistance of the foam matrix in horizontal direction becomes more obvious.

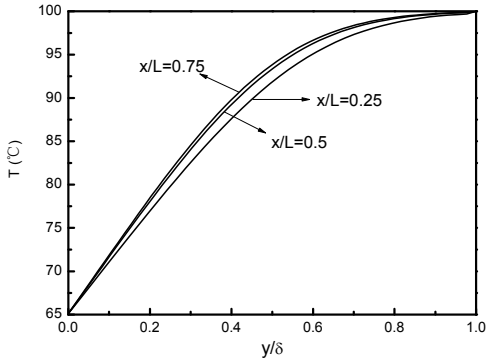

Fig. 20. Temperature distribution in condensate layer for different x (ε =0.9, 10 PPI)

Effects of parameters involving Jacobi number, porosity, and pore density are discussed in this section. Super cooling degree can be controlled by changing the value of Ja. The effect of Ja on the condensate layer thickness is shown in Fig. 21(a). It can be seen that condensate

layer thickness decreases as the Jacobi number increases. This can be attributed to the fact that the super cooling degree, which is the key factor driving the condensation process, is reduced as the ***Ja*** number increases, leading to a thinner liquid condensate layer. For a limited case of zero super cooling degree, condensation cannot occur and the condensate layer does not exist.

The effect of porosity on the condensate film thickness is shown in Fig. 21(b). It is found that in a fixed position, increase in porosity can lead to the decrease in the condensate film thickness, which is helpful for film condensation. This can be attributed to the fact that the increase in porosity can make the permeability of the metallic foams increase, decreasing the flow resistance of liquid flowing downwards. The effect of pore density on the condensate film thickness is shown in Fig. 21(c). It can be seen that for a fixed x position, the increase in pore density can make the condensate film thickness increase greatly, which enlarges the thermal resistance of the condensation heat transfer process. The reason for the above result is that the increasing pore density can significantly reduce metal foam permeability and substantially increase the flow resistance of the flowing-down condensate. Thus, with either an increase in porosity or a decrease in pore density, condensate layer thickness is reduced for condensation heat transfer coefficient.

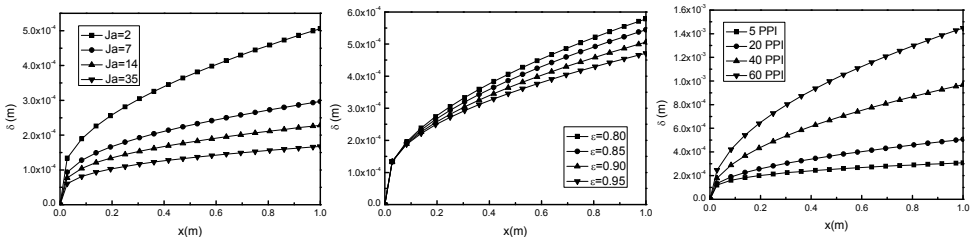

(a) (b) (c)

Fig. 21. Effects of important parameters on condensate thickness distribution: (a) effect of Jacobi number (ε =0.9, 10 PPI); (b) effect of porosity (10PPI); (c) pore density (ε =0.9)

5. Conclusion

Metallic porous media exhibit great potential in heat transfer area. The characteristic of high pressure drop renders those with high porosity and low pore density considerably more attractive in view of pressure loss reduction. For forced convective heat transfer, another way to lower pressure drop is to fill the duct partially with metallic porous media.

In this chapter, natural convection in metallic foams is firstly presented. Their enhancement effects on heat transfer are moderate. Next, we exhibit theoretical modeling on thermal performance of metallic foam fully/partially filled duct for internal flow with the two-equation model for high solid thermal conductivity foams. Subsequently, a numerical model for film condensation on a vertical plate embedded in metallic foams is presented and the effects of advection and inertial force are considered, which are responsible for the non-linear effect of cross-sectional temperature distribution. Future research should be focused on following areas with metallic porous media: implementation of computation and parameter optimization for practical design of thermal application, phase change process, turbulent flow and heat transfer, non-equilibrium conjugate heat transfer at porous-fluid

interface, thermal radiation, experimental data/theoretical model/flow regimes for two-phase/multiphase flow and heat transfer, and so on.

6. Acknowledgment

This work is supported by the National Natural Science Foundation of China (No. 50806057), the National Key Projects of Fundamental R/D of China (973 Project: 2011CB610306), the Ph.D. Programs Foundation of the Ministry of Education of China (200806981013) and the Fundamental Research Funds for the Central Universities.

7. References

Alazmi, B. & Vafai, K. (2001). Analysis of Fluid Flow and Heat Transfer Interfacial Conditions Between a Porous Medium and a Fluid Layer. *International Journal of Heat and Mass Transfer*, Vol.44, No.9, (May 2001), pp. 1735-1749, ISSN 0017-9310

Al-Nimer, M.A. & Al-Kam, M.K. (1997). Film Condensation on a Vertical Plate Imbedded in a Porous Medium. *Applied Energy*, Vol. 56, No.1, (January 1997), pp. 47-57, ISSN 0306-2619

Banhart, J. (2001). Manufacture, characterisation and application of cellular metals and metal foams, *Progress in Materials Science*, Vol.46, No.6, (2001), pp. 559-632, ISSN 0079-6425

Boomsma, K. &Poulikakos, D. (2001). On the Effective Thermal Conductivity of a Three-Dimensionally Structured Fluid-Saturated Metal Foam. *International Journal of Heat and Mass Transfer*, Vol.44, No.4, (February 2001), pp. 827-836, ISSN 0017-9310

Calmidi, V.V. (1998). *Transport phenomena in high porosity fibrous metal foams*. Ph.D. thesis, University of Colorado.

Calmidi, V.V. & Mahajan, R.L. (2000). Forced convection in high porosity metal foams. *Journal of Heat Transfer*, Vol.122, No.3, (August 2000), pp. 557-565, ISSN 0022-1481

Chang, T.B. (2008). Laminar Film Condensation on a Horizontal Wavy Plate Embedded in a Porous Medium. *International Journal of Thermal Sciences*, Vol. 47, No.4, (January 2008), pp. 35–42, ISSN 1290-0729

Cheng, B. & Tao, W.Q. (1994). Experimental Study on R-152a Film Condensation on Single Horizontal Smooth Tube and Enhanced Tubes. *Journal of Heat Transfer*, Vol.116, No.1, (February 1994), pp. 266-270, ISSN 0022-1481

Cheng, P. & Chui, D.K. (1984). Transient Film Condensation on a Vertical Surface in a Porous Medium. *International Journal of Heat and Mass Transfer*, Vol.27, No.5, (May 1984), pp. 795–798, ISSN 0017-9310

Churchil S.W. & Ozoe H. (1973). A Correlation for Laminar Free Convection from a Vertical Plate. *Journal of Heat Transfer*, Vol.95, No.4, (November 1973), pp. 540-541, ISSN 0022-1481

Dhir, V.K. & Lienhard, J.H. (1971). Laminar Film Condensation on Plane and Axisymmetric Bodies in Nonuniform Gravity. *Journal of Heat Transfer*, Vol.93, No.1, (February 1971), pp. 97-100, ISSN 0022-1481

Du, Y.P.; Qu, Z.G.; Zhao, C.Y. &Tao, W.Q. (2010). Numerical Study of Conjugated Heat Transfer in Metal Foam Filled Double-Pipe. *International Journal of Heat and Mass Transfer*, Vol.53, No.21, (October 2010), pp. 4899-4907, ISSN 0017-9310

Du, Y.P.; Qu, Z.G.; Xu, H.J.; Li, Z.Y.; Zhao, C.Y. &Tao, W.Q. (2011). Numerical Simulation of Film Condensation on Vertical Plate Embedded in Metallic Foams. *Progress in Computational Fluid Dynamics*, Vol.11, No.3-4, (June 2011), pp. 261-267, ISSN 1468-4349

Dukhan, N. (2009). Developing Nonthermal-Equilibrium Convection in Porous Media with Negligible Fluid Conduction. *Journal of Heat Transfer*, Vol.131, No.1, (January 2009), pp. 014501.1-01450.3, ISSN 0022-1481

Fujii T. & Fujii M. (1976). The Dependence of Local Nusselt Number on Prandtl Number in Case of Free Convection Along a Vertical Surface with Uniform Heat-Flux. *International Journal of Heat and Mass Transfer*, Vol. 19, No.1, (January 1976), pp. 121-122, ISSN 0017-9310

Incropera, F.P.; Dewitt, D.P. & Bergman, T.L. (1985). *Fundamentals of heat and mass transfer* (2nd Edition), ISBN 3540295267, Springer, New York, USA

Jain, K.C. & Bankoff, S.G. (1964). Laminar Film Condensation on a Porous Vertical Wall with Uniform Suction Velocity. *Journal of Heat Transfer*, Vol. 86, (1964), pp. 481-489, ISSN 0022-1481

Jamin Y.L. & Mohamad A.A. (2008). Natural Convection Heat Transfer Enhancements From a Cylinder Using Porous Carbon Foam: Experimental Study. *Journal of Heat Transfer*, Vol.130, No.12, (December 2008), pp. 122502.1-122502.6, ISSN 0022-1481

Lee, D.Y. & Vafai, K. (1999). Analytical characterization and conceptual assessment of solid and fluid temperature differentials in porous media. *International Journal of Heat and Mass Transfer*, Vol.42, No.3, (February 1999), pp. 423-435, ISSN 0017-9310

Lienhard, J.H. IV & Lienhard J.H.V (2006). *A heat transfer textbook* (3rd Edition), Phlogiston, ISBN 0-15-748821-1, Cambridge in Massachusetts, USA

Lu, T.J.; Stone, H.A. & Ashby, M.F. (1998). Heat transfer in open-cell metal foams. *Acta Materialia*, Vol.46, No.10, (June 1998), pp. 3619-3635, ISSN 1359-6454

Lu, W.; Zhao, C.Y. & Tassou, S.A. (2006). Thermal analysis on metal-foam filled heat exchangers, Part I: Metal-foam filled pipes. *International Journal of Heat and Mass Transfer*, Vol.49, No.15-16, (July 2006), pp. 2751-2761, ISSN 0017-9310

Mahjoob, S. & Vafai, K. (2009). Analytical Characterization of Heat Transport through Biological Media Incorporating Hyperthermia Treatment. *International Journal of Heat and Mass Transfer*, Vol.52, No.5-6, (February 2009), pp. 1608–1618, ISSN 0017-9310

Masoud, S.; Al-Nimr, M.A. & Alkam, M. (2000). Transient Film Condensation on a Vertical Plate Imbedded in Porous Medium. *Transport in Porous Media*, Vol. 40, No.3, (September 2000), pp. 345–354, ISSN 0169-3913

Nusslet, W. (1916). Die Oberflachenkondensation des Wasserdampfes. *Zeitschrift des Vereines Deutscher Ingenieure*, Vol. 60, (1916), pp. 541-569, ISSN 0341-7255

Ochoa-Tapia, J.A. & Whitaker, S. (1995). Momentum Transfer at the Boundary Between a Porous Medium and a Homogeneous Fluid-I: Theoretical Development. *International Journal of Heat and Mass Transfer*, Vol.38, No.14, (September 1995), pp. 2635-2646, ISSN 0017-9310

Phanikumar, M.S. & Mahajan, R.L. (2002). Non-Darcy Natural Convection in High Porosity Metal Foams. *International Journal of Heat and Mass Transfer*, Vol.45, No.18, (August 2002), pp. 3781–3793, ISSN 0017-9310

Popiel, C.O. & Boguslawski, L. (1975). Heat transfer by laminar film condensation on sphere surfaces. *International Journal of Heat and Mass Transfer*, Vol.18, No.12, (December 1975), pp. 1486-1488, ISSN 0017-9310

Poulikakos, D. & Kazmierczak, M. (1987). Forced Convection in Duct Partially Filled with a Porous Material. *Journal of Heat Transfer*, Vol.109, No.3, (August 1987), pp. 653-662, ISSN 0022-1481

Sparrow E.M. & Gregg, J.L. (1956). Laminar free convection from a vertical plate with uniform surface heat flux. *Transactions of ASME*, Vol. 78, (1956), pp. 435-440

Sukhatme, S.P.; Jagadish, B.S. & Prabhakaran P. (1990). Film Condensation of R-11 Vapor on Single Horizontal Enhanced Condenser Tubes. *Journal of Heat Transfer*, Vol. 112, No.1, (February 1990), pp. 229-234, ISSN 0022-1481

Tao, W.Q. (2005). *Numerical Heat Transfer* (2nd Edition), Xi'an Jiaotong University Press, ISBN 7-5605-0183-4, Xi'an, China.

Wang, S.C.; Chen, C.K. & Yang, Y.T. (2006). Steady Filmwise Condensation with Suction on a Finite-Size Horizontal Plate Embedded in a Porous Medium Based on Brinkman and Darcy models. *International Journal of Thermal Science*, Vol.45, No.4, (April 2006), pp. 367–377, ISSN 1290-0729

Wang, S.C.; Yang, Y.T. & Chen, C.K. (2003). Effect of Uniform Suction on Laminar Film-Wise Condensation on a Finite-Size Horizontal Flat Surface in a Porous Medium. *International Journal of Heat and Mass Transfer*, Vol.46, No.21, (October 2003), pp. 4003-4011, ISSN 0017-9310

Xu, H.J.; Qu, Z.G. & Tao, W.Q. (2011a). Analytical Solution of Forced Convective Heat Transfer in Tubes Partially Filled with Metallic Foam Using the Two-equation Model. *International Journal of Heat and Mass Transfer*, Vol. 54, No.17-18, (May 2011), pp. 3846–3855, ISSN 0017-9310

Xu, H.J.; Qu, Z.G. & Tao, W.Q. (2011b). Thermal Transport Analysis in Parallel-plate Channel Filled with Open-celled Metallic Foams. *International Communications in Heat and Mass Transfer*, Vol.38, No.7, (August 2011), pp. 868-873, ISSN 0735-1933

Xu, H.J.; Qu, Z.G.; Lu, T.J.; He, Y.L. & Tao, W.Q. (2011c). Thermal Modeling of Forced Convection in a Parallel Plate Channel Partially Filled with Metallic Foams. *Journal of Heat Transfer*, Vol.133, No.9, (September 2011), pp. 092603.1-092603.9, ISSN 0022-1481

Zhao, C.Y.; Kim, T.; Lu, T.J. & Hodson, H.P. (2001). *Thermal Transport Phenomena in Porvair Metal Foams and Sintered Beds*. Technical report, University of Cambridge.

Zhao, C.Y.; Kim, T.; Lu, T.J. & Hodson, H.P. (2004). Thermal Transport in High Porosity Cellular Metal Foams. *Journal of Thermophysics and Heat Transfer*, Vol.18, No.3, (2004), pp. 309-317, ISSN 0887-8722

Zhao, C.Y.; Lu, T.J. & Hodson, H.P. (2004). Thermal radiation in ultralight metal foams with open cells. *International Journal of Heat and Mass Transfer*, Vol. 47, No.14-16, (July 2004), pp. 2927–2939, ISSN 0017-9310

Zhao, C.Y.; Lu, T.J. & Hodson, H.P. (2005). Natural Convection in Metal Foams with Open Cells. *International Journal of Heat and Mass Transfer*, Vol.48, No.12, (June 2005), pp. 2452–2463, ISSN 0017-9310

Zhao, C.Y.; Lu, W. & Tassou, S.A. (2006). Thermal analysis on metal-foam filled heat exchangers, Part II: Tube heat exchangers. *International Journal of Heat and Mass Transfer*, Vol.49, No.15-16, (July 2006), pp. 2762-2770, ISSN 0017-9310

Heat Transfer - Engineering Applications

Edited by Prof. Vyacheslav Vikhrenko

ISBN 978-953-307-361-3
Hard cover, 400 pages
Publisher InTech
Published online 22, December, 2011
Published in print edition December, 2011

Heat transfer is involved in numerous industrial technologies. This interdisciplinary book comprises 16 chapters dealing with combined action of heat transfer and concomitant processes. Five chapters of its first section discuss heat effects due to laser, ion and plasma-solid interaction. In eight chapters of the second section engineering applications of heat conduction equations to the curing reaction kinetics in manufacturing process, their combination with mass transport or ohmic and dielectric losses, heat conduction in metallic porous media and power cables are considered. Analysis of the safety of mine hoist under influence of heat produced by mechanical friction, heat transfer in boilers and internal combustion engine chambers, management for ultrahigh strength steel manufacturing are described in this section as well. Three chapters of the last third section are devoted to air cooling of electronic devices.

InTech Europe
University Campus STeP Ri
Slavka Krautzeka 83/A
51000 Rijeka, Croatia
Phone: +385 (51) 770 447
Fax: +385 (51) 686 166
www.intechopen.com

InTech China
Unit 405, Office Block, Hotel Equatorial Shanghai
No.65, Yan An Road (West), Shanghai, 200040, China
中国上海市延安西路65号上海国际贵都大饭店办公楼405单元
Phone: +86-21-62489820
Fax: +86-21-62489821